Identifying Interstellar Object Impact Craters

Samuel H. C. Cabot and Gregory Laughlin
Yale University, 52 Hillhouse, New Haven, CT 06511, USA; sam.cabot@yale.edu

Abstract

The discoveries of two interstellar objects (ISOs) in recent years have generated significant interest in constraining their physical properties and the mechanisms behind their formation. However, their ephemeral passages through our solar system permitted only incomplete characterization. We investigate avenues for identifying craters that may have been produced by ISOs impacting terrestrial solar system bodies, with particular attention toward the Moon. A distinctive feature of ISOs is their relatively high encounter velocity compared to asteroids and comets. Local stellar kinematics indicate that terrestrial solar system bodies should have experienced of order unity ISO impacts exceeding $100 \, \mathrm{km \, s^{-1}}$. By running hydrodynamical simulations for projectiles of different masses and impact velocities up to $100 \, \mathrm{km \, s^{-1}}$, we show how late-stage equivalence dictates that transient crater dimensions alone are insufficient for inferring the projectile's velocity. On the other hand, the melt volume within craters of a fixed diameter may be a potential route for identifying ISO craters, as faster impacts produce more melt. This method requires that the melt volume scales with the energy of the projectile while the crater diameter scales with the point-source limit (subenergy). Given that there are probably only a few ISO craters in the solar system at best, and that transient crater dimensions are not a distinguishing feature for impact velocities, at least up to $100 \, \mathrm{km \, s^{-1}}$, identification of an ISO crater proves a challenging task. Melt volume and high-pressure petrology may be diagnostic features once large volumes of material can be analyzed in situ.

1. Introduction

The discoveries of 'Oumuamua (from the Pan-STARRS survey; Meech et al. 2017) and comet 2I/Borisov (by G. Borisov at the Crimean Astrophysical Observatory in 2019)[1] have prompted intensive study of the number density, composition, and origin of interstellar objects (ISOs). Initial upper limits on number density were placed by Engelhardt et al. (2017) based on simulated ISO populations and their detectability by modern surveys. However, the discovery of 'Oumuamua yielded an estimate for similar objects of $0.2 \, \mathrm{au^{-3}}$ (Do et al. 2018). While comet 2I/Borisov is very similar to solar system comets (Guzik et al. 2020), 'Oumuamua's oblong shape and lack of a coma (Meech et al. 2017), along with its anomalous acceleration (Micheli et al. 2018), have forced reconsideration of its makeup, including materials atypical of comets and asteroids (e.g., Füglistaler & Pfenniger 2018; Rafikov 2018; Desch & Jackson 2021). Earlier identification with the Vera C. Rubin Observatory (LSST) or even in situ analyses (Snodgrass & Jones 2019) would drastically improve our understanding of ISOs, specifically, their relationship to the galaxy-wide population of ejected planetesimals (Trilling et al. 2017).

The entry trajectory of 'Oumuamua (at speed $v_\infty \simeq 26 \, \mathrm{km \, s^{-1}}$; Meech et al. 2017) was similar to the local standard of rest (LSR; Francis & Anderson 2009), consistent with expectations for ISOs. The difference between the median velocity of nearby stars (XHIP catalog; Anderson & Francis 2012) and that of 'Oumuamua's entry was only about $4.5 \, \mathrm{km \, s^{-1}}$ at $\sim 6°$ (Mamajek 2017). Nevertheless, 'Oumuamua was not comoving with any particular nearby system. While specific stars have been postulated as the origin, chaotic gravitational interactions make a precise back-tracing impossible. Unexpectedly perhaps, 2I/Borisov entered at $v_\infty \sim 32 \, \mathrm{km \, s^{-1}}$ at $\sim 75°$ away from the solar apex (Guzik et al. 2020), its origin again speculative (Dybczyński et al. 2019). As pointed out by Do et al. (2018), the detection volume of ISOs scales as v_∞^{-1} from multiplication between gravitational focusing from the Sun (the effective cross section becomes $r_g^2 = r^2[(v_{\mathrm{esc}}/v_\infty)^2 + 1]$) with the impingement rate. Therefore, ISOs may be less efficiently detected if they encounter the solar system at speeds substantially exceeding the Sun's escape velocity at $d \sim 1 \, \mathrm{au}$. The detectability of ISOs as a function of v_∞ and impact parameter b was quantified by Seligman & Laughlin (2018). The ISOs with $v_\infty \gtrsim 10 \, \mathrm{km \, s^{-1}}$ must have $b \lesssim 5 \, \mathrm{au}$ if they are to be identified by LSST prior to periastron. Although 'Oumuamua came serendipitously close to Earth ($r_p \simeq 0.25 \, \mathrm{au}$, $b \simeq 0.85 \, \mathrm{au}$), these calculations reveal the significant challenge of detecting additional ISOs.

Motivated by an encouragingly high encounter rate of ISOs, up to $\sim$seven per year, that pass within 1 au of the Sun (Eubanks et al. 2021), we consider an alternative route to characterizing these enigmatic objects: identifying ISO impact craters on terrestrial solar system bodies. For example, molten and vaporized projectile matter may mix with impact-modified target rock (impactites) and impart telltale chemical signatures. More optimistically, some projectile material might survive in solid phase. A suite of standard chemical and isotopic analyses exists for characterizing meteorites and impact melts (Tagle & Hecht 2006; Joy et al. 2016), which could reveal the ISO's composition.

---

[1] www.minorplanetcenter.net/mpec/K19/K19RA6.html

Before an in situ or retrieved sample analysis is possible, we need a high-fidelity method for screening ISO craters from asteroid and comet craters. Crater morphology and high-pressure petrology may be differentiating traits, but this premise is significantly challenged by well-known degeneracies between crater and projectile properties (Dienes & Walsh 1970; Holsapple & Schmidt 1982). However, some constraints have been achieved for especially renowned and well-studied craters. For example, Collins et al. (2020) used 3D simulations to link asymmetries in the Chicxulub crater to a steeply inclined impact trajectory, though the observations are compatible with a modest range of angles and impact speeds. Using an atmospheric-entry fragmentation model, Melosh & Collins (2005) posited that Meteor Crater was formed by a low-speed impact, which additionally explains an anomalously low melt volume. However, this model was challenged by Artemieva & Pierazzo (2011) on the basis of little observed solid projectile ejecta. As another example, Johnson et al. (2016) modeled the formation of the Sputnik Planum basin and found consistency with a 220 km diameter projectile; however, they assumed a $2 \, \text{km s}^{-1}$ speed typical for impacts on Pluto. There is a considerable amount of literature surrounding each of these craters, which raises a number of other interpretations than those listed here (e.g., Artemieva & Pierazzo 2009; Denton et al. 2021) and echoes the difficulties of inferring projectile properties from their craters. We note that impacts in the solar system virtually never exceed $\gtrsim 100 \, \text{km s}^{-1}$; hence, these speeds are seldom modeled in the literature. Nevertheless, we will show that they are not atypical for ISO impacts and thus warrant further investigation; this aspect is the main focus of our study.

If ISO craters can be identified, then surviving ISO meteorites in and around the crater could be readily analyzed for metallic content, oxygen isotope fractionation, and elemental ratios (e.g., Fe/Mn; Joy et al. 2016); however, if ISOs are composed of highly volatile, exotic ice (Seligman & Laughlin 2020; Desch & Jackson 2021), we may expect that they undergo near-complete vaporization upon impact and suffer the same issues in chemical-based identification as comets do (Tagle & Hecht 2006; a small percentage of water content may survive comet impacts; Svetsov & Shuvalov 2015). An ISO's composition could still be investigated if its material persists in the impact melt or vapor condensates. For example, Tagle & Hecht (2006) evaluated a few methods for projectile classification involving relative concentrations of platinum group elements (PGEs), Ni and Cr, and isotopic ratios of Cr and Os. At present, 'Oumuamua's composition is highly speculative, as is the composition of the general ISO population. Any insight into their compositions can be directly tied to formation pathways (e.g., molecular cloud cores in the case of H_2 or cratered ice sheets in the case of N_2), as well as their abundance in the galaxy (Levine et al. 2021, and references therein).

Our study is outlined as follows. In Section 2, we review the impingement rate of ISOs and the expected velocity distribution based on local stellar kinematics. In Section 3, we present hydrodynamical simulations representative of ISO impacts on terrestrial bodies. While certain aspects of these impacts are unconstrained (most notably the projectile composition), we use well-understood materials as proxies to obtain order-of-magnitude estimates of crater size and melt volume. We restrict the analysis to transient craters for simplicity, although collapse and viscous degradation may modify their shapes (Melosh 1989,

Chapter 8). Specific attention is given to lunar cratering in light of soon-to-be-realized exploration missions; however, parts of our investigation extend to other terrestrial bodies, such as Mars. The simulation results are subsequently compared to predictions from crater scaling relationships. We discuss additional scaling relations in Section 4, with a particular focus on how melt volume may be used to infer the impact velocity. Our results are summarized in Section 5.

2. ISO Impact Velocities

It is important to determine the speed at which ISOs impact terrestrial bodies in the solar system. A significant component is from v_∞, the speed at which the ISO encounters the solar system. About $40 \, \text{km s}^{-1}$ is added in quadrature for ISOs that come within 1 au of the Sun. The ISO impacts on the Moon can reach velocities $\geqslant 100 \, \text{km s}^{-1}$; these events are the focus of our study. We review analytic expressions for the kinematics of stars in the solar neighborhood, as well as measurements of the velocity dispersion along each principal axis. Next, we independently analyze the kinematics of stars with full phase-space measurements provided in the recent Gaia data release. These velocities are combined with the estimated number density of ISOs to obtain the encounter rate as a function of ISO speed.

2.1. Local Stellar Kinematics: Theory

The ISOs of icy composition are expected to have a kinematic distribution reflective of their origin systems. Binney & Tremaine (2008) showed that velocities in the galactic disk are well described by a Schwarzschild distribution,

$$f(\mathbf{v}) = S(L_z)\exp\left[-\left(\frac{v_R^2 + \gamma^2\tilde{v}_\phi^2}{2\sigma_R^2(L_z)} + \frac{v_z^2 + 2\Phi_z(z, L_z)}{2\sigma_z^2(L_z)}\right)\right],$$ (1)

for cylindrical velocity components v_R, v_ϕ, and v_z and their respective dispersions, σ_R, σ_ϕ, and σ_z (Dehnen & Binney 1998; Nordström et al. 2004). Angular momentum is denoted as L_z. The term $\tilde{v}_\phi \equiv v_\phi - v_c(R)\hat{e}_\phi$ represents the difference between the angular velocity component and the circular velocity at the star's galactic radius, R. The term $\gamma \equiv 2\Omega/\kappa$ arises from the guiding center approximation, where Ω is the circular frequency and κ is the epicyclic frequency. The potential $\Phi_z(z, L_z)$ appears from an approximation to the third integral of motion. The exponential form follows from Shu (1969), and the leading term $S(L_z)$ depends on the surface density of stars. Under two approximations—first, that the surface density follows an exponential disk, and second, that the dispersions are relatively low compared to the circular speed (i.e., that the stars are of a "cold" population)—the solar neighborhood distribution follows a triaxial Gaussian model (Schwarzschild 1907),

$$dn \propto \exp\left[-\left(\frac{v_R^2 + \gamma^2\tilde{v}_\phi^2}{2\sigma_R^2} + \frac{v_z^2}{2\sigma_z^2}\right)\right].$$ (2)

If one generalizes beyond the epicyclic approximation, which also assumed that $\sigma_\phi/\sigma_R = \kappa/2\Omega$, then the solar

neighborhood distribution becomes

$$f(\mathbf{v})d^3\mathbf{v} = \frac{n_0 d^3\mathbf{v}}{(2\pi)^{3/2}\sigma_R\sigma_\phi\sigma_z}\exp\left[-\left(\frac{v_R^2}{2\sigma_R^2} + \frac{\tilde{v}_\phi^2}{2\sigma_\phi^2} + \frac{v_z^2}{2\sigma_z^2}\right)\right],$$

(3)

where n_0 is the number of stars per unit volume (Binney & Tremaine 2008). This equation is useful under the assumption that ISOs originate predominantly from nearby Population I stars. As discussed in the following subsection, population studies provide excellent constraints on the dispersion along each principal axis. However, the distribution for speed $|v|$ is not well described by a Gaussian or Boltzmann distribution; a lognormal model provides a reasonable fit (Eubanks et al. 2021).

The impact rate of ISOs, $\Gamma = n_{ISO}\sigma_p v_\infty$, depends on the number density of ISOs, the cross-sectional area of the target, and the relative velocity of the two bodies. A more detailed formulation is given by Lacki (2021),

$$\Gamma(\geqslant K_T) = \int_0^\infty \int_{2K_T/v_\infty}^\infty \sigma_p v_\infty f(v_\infty)\frac{dn_{ISO}}{dm}dm dv_\infty,$$

(4)

which is the impact rate of ISOs with energy at least K_T. The mass distribution is probably well described by a power law, which is often adopted for minor-body populations in the solar system. Order-of-magnitude estimates by Lacki (2021) yield an ISO impact rate of 6×10^{-6} Gyr^{-1} at Earth, restricted to projectiles with $\geqslant 1$ YJ kinetic energy (roughly equivalent a 10^{15} kg projectile impacting at 45 km s^{-1}). A 1D Maxwellian stellar velocity dispersion of 30 km s^{-1} was assumed, which is roughly the average of the three solar neighborhood dispersions measured by Anguiano et al. (2017). We investigate the local velocity dispersion in more detail in the next subsection. Note that the actual impact speed of the ISO is higher than the relative speed with the solar system ($v_i > v_\infty$) due to extra energy gained by falling into the Sun's potential well, plus a small contribution from the target planet or satellite's gravity, notwithstanding atmospheric effects. Also, the effective cross section is modified by gravitational focusing.

Our investigation hinges on the possibility that anomalously fast ISO impacts produce craters distinct from comet and asteroid impacts. Therefore, we review the distributions of impact speeds in the solar system to determine a velocity threshold that effectively excludes comets and asteroids. Impacts at Earth, Venus, and Mercury commonly exceed 20 km s^{-1} (Le Feuvre & Wieczorek 2011), with Mercury's distribution extending to 90 km s^{-1}. For the Earth/Moon system, impacts rarely occur at greater than 50 km s^{-1} (Le Feuvre & Wieczorek 2011). The high-velocity tail mainly comprises long-period comets that may impact at speeds up to $\sim$70 km s^{-1} (Steel 1998). The cosmic velocities of ISOs, however, occasionally exceed 90 km s^{-1} (see below) and would therefore yield impacts faster than expected for typical solar system impactors (e.g., 100 km s^{-1} at Earth and up to 113 km s^{-1} at Mercury, taking into account the Sun's potential well and planet escape velocity). Comet and asteroid impact velocities are generally lower for bodies at larger semimajor axes. For example, the mean impact speed is 10.6 km s^{-1} for Mars (Le Feuvre & Wieczorek 2008) and 4.75 km s^{-1} for Vesta (O'Brien & Sykes 2011). The distribution of impacts vanishes past 40 km s^{-1} for Mars and 12 km s^{-1} for Vesta and Ceres (O'Brien & Sykes 2011). If craters could be linked to these impact speeds or higher, ISOs would be strong candidates for the associated projectile. Therefore, while this study is primarily concerned with impacts on the Moon, a larger range in impact speed could be associated with ISOs for craters on Mars and more distant terrestrial bodies.

2.2. Local Stellar Kinematics: Observed

The proper motions of nearby stars are thoroughly measured thanks to large surveys. Gaia, for example, has provided a massive catalog of 7.2 million stars with complementary line-of-sight velocities (Gaia Collaboration et al. 2018). After filtering, their main sample contained approximately 6.4 million sources with full phase-space measurements. The vast majority of stars within the sample lie near the origin in the classic Toomre diagram (Sandage & Fouts 1987) depicting V against $(U^2 + W^2)^{1/2}$ offset by the solar LSR (U, V, and W refer to radial, tangential, and vertical velocity components, respectively). This figure is often used to depict distinct populations of stars (Venn et al. 2004). Isovelocity contours in the Toomre diagram delineate transitions between stellar populations; for example, Nissen (2004) defined 80 and 180 km s^{-1} as the boundaries confining thick-disk stars, where lower speeds correspond to thin-disk stars. Venn et al. (2004) used the Toomre diagram to dynamically classify stars into five categories (thin-disk, thick-disk, halo, high-velocity, and retrograde) and subsequently determine the chemical properties of each population.

A significant fraction of stars in the Gaia catalog have relative speeds exceeding 100 km s^{-1}, but few lie in the solar system's vicinity. For stars in the galactic midplane (extending -200 to $+200$ pc), velocity dispersions are of order 10–40 km s^{-1} for the three components, with some variation in radial distance from the galactic center. Populations of stars that are a few kiloparsecs above and below the midplane exhibit dispersions of up to 60–80 km s^{-1} per component. Other survey studies also report the spatial dependence of velocity dispersion (generally increasing toward the galactic center and away from the midplane; e.g., Bond et al. 2010; Recio-Blanco et al. 2014). Stellar properties such as metallicity and age are correlated with velocity dispersion (e.g., Stromgren 1987; Nissen 2004; Rojas-Arriagada et al. 2014). Example dispersions considered by Binney & Tremaine (2008) were based on the Geneva–Copenhagen survey (Nordström et al. 2004) that observed F and G dwarfs. Nordström et al. (2004) presented age-dependent velocity dispersions. The youngest stars (within their 1 Myr age bin) had $\sigma_{tot} \approx 30$ km s^{-1}, while the oldest stars (within their 10 Myr age bin) had $\sigma_{tot} \approx 60$ km s^{-1}. In all bins, it was found that $\sigma_U > \sigma_V > \sigma_W$.

We analyzed the dynamics of ISOs originating within the local stellar neighborhood using Gaia EDR3 data (Gaia Collaboration et al. 2021) in a similar fashion as Marchetti (2021) and Eubanks et al. (2021). The Sun's peculiar velocity was taken as (11.1, 12.24, 7.25) km s^{-1} (Schönrich et al. 2010) relative to an LSR of (0, 235, 0) km s^{-1}. The dynamics of the closest stars are probably most representative of ISO velocities, so we included only stars within 200 pc of the Sun. The Toomre diagram for the stellar sample is shown in Figure 1, where the velocity components are as measured in the Sun's rest frame. Each bin is rescaled to reflect its contribution to the encounter rate of ISOs. This step is accomplished by first
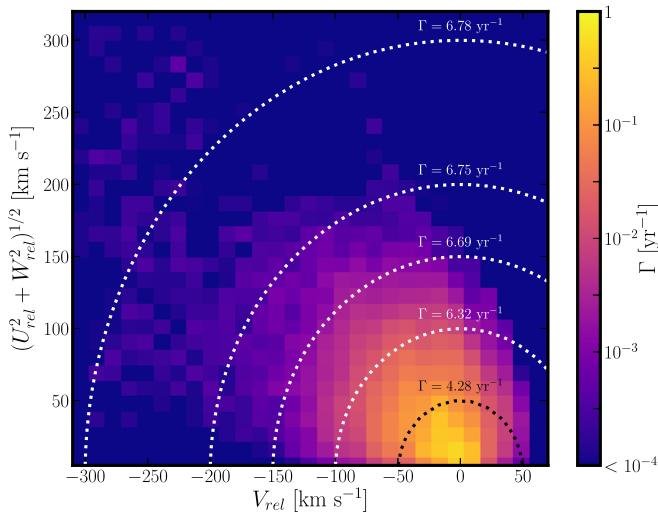
Figure 1. Toomre diagram for Gaia EDR3 stars within 200 pc of the Sun, which have full phase-space measurements. The origin represents the rest frame of the Sun. Values have been normalized to depict the encounter rate of ISOs within 1 au of the Sun. Curves correspond to, from innermost to outermost, constant encounter speeds of 50, 100, 150, 200, and 300 km s^{-1}. Labels indicate the summed encounter rate of all ISOs with velocities enclosed by the curve.

normalizing the sum over all bins to the ISO number density, $n_{\rm ISO} \sim 0.1$ au^{-3}. This value is half the estimate of Do et al. (2018) and used as an upper limit by Eubanks et al. (2021), who appealed to the lack of recent detections. Each bin is multiplied by its speed, $|v_\infty| = \sqrt{U_{\rm rel}^2 + V_{\rm rel}^2 + W_{\rm rel}^2}$; a cross section of 1 au^2; and a gravitational-focusing enhancement factor of $1 + (v_{\rm esc}/v_\infty)^2$, where $v_{\rm esc}$ is evaluated at 1 au. The results do not strongly depend on population volume, since we normalize the distribution to reflect the total number density of ISOs. We find that the total encounter rate of ISOs within 1 au of the Sun is about 6.80 yr^{-1}. The majority arrive with $v_\infty < 100$ km s^{-1}, with a rate of 6.32 yr^{-1}. High-speed ISOs with $v_\infty > 100$ km s^{-1} arrive at 0.47 yr^{-1}, and $v_\infty > 200$ km s^{-1} arrive at 0.05 yr^{-1}. Our results are nearly the same as those of Eubanks et al. (2021).

Interestingly, high-speed ISOs make a nonnegligible contribution to the encounter rate, despite the vast majority of nearby stars having relative speeds of $\lesssim 100$ km s^{-1} (the peak of the distribution lies at around 40 km s^{-1}). Multiplying by the ratio of the target's cross section to 1 au^2, we find that Earth and the Moon experience ~ 12 and ~ 0.9 ISO impacts Gyr^{-1}, respectively. The objects most pertinent to this study, ISOs that impact the the Moon at speeds of $v_i > 100$ km s^{-1}, have encounter speeds of $v_\infty > 90.6$ km s^{-1} and a corresponding impact rate of ~ 0.09 Gyr^{-1}. Equivalently, there is a 31% chance that the Moon experienced a high-speed ISO impact in the past 4 Gyr. Repeating the above analysis for Mars yields a high-speed impact rate of ~ 0.29 Gyr^{-1}. These results indicate that there should be of order unity high-speed ISO impact craters on the Moon and Mars.

For most remaining terrestrial bodies, the chances of identifying an ISO crater based on the projectile's extreme speed appear slim. High-speed impacts of asteroids and comets are common at Mercury's orbit (Le Feuvre & Wieczorek 2011), Venus experienced a recent cataclysmic resurfacing event (Schaber et al. 1992), and Earth's geological activity has largely erased ancient craters. The Galilean Moons Io and Europa seem unlikely candidates due to their small surface areas and young surface ages of 0.3–2.3 and 60 Myr, respectively (Schenk et al. 2004). Ganymede and Callisto, on the other hand, have surface ages of $\gtrsim 2$ Gyr and could be potential targets.

3. Transient Crater Dimensions

It is well known that crater dimensions are highly degenerate with projectile properties (e.g., velocity, radius, density, and impact angle; Dienes & Walsh 1970; Holsapple & Schmidt 1987). We simulate impacts on the Moon in order to test whether degeneracies persist at the high-velocity tail of ISO impacts. Our selection of target materials is a subset of those simulated by Prieur et al. (2017), characteristic of the lunar regolith and upper megaregolith. We then compare the results to theoretical expectations for crater diameter based on late-stage equivalence (Dienes & Walsh 1970).

3.1. Simulation Overview

We simulate impacts with the iSALE-Dellen 2D hydrocode (Wünnemann et al. 2006), which is based on the Simplified Arbitrary Lagrangian-Eulerian (SALE) program (Amsden et al. 1980) designed for fluid flow at all speeds. SALE features a Lagrangian update step, an implicit update for time-advanced pressure and velocity fields, and an advective flux step for Eulerian simulations. Calculations are performed on a mesh in an Eulerian frame of reference to prevent highly distorted cells. Over the years, the program has seen new physics implemented, including an elastoplastic constitutive model, fragmentation models, various equations of state (EoSs), multiple materials, and new models of strength, porosity compaction, and dilatancy (Melosh et al. 1992; Ivanov et al. 1997; Wünnemann et al. 2006; Collins et al. 2011; Collins 2014). Massless tracer particles moving within the mesh (Pierazzo et al. 1997) record relevant Lagrangian fields. We adopt a resolution of 20 cells per projectile radius (CPPR), which has been demonstrated to be within $\sim 10\%$ of the convergent spall velocity (Head et al. 2002), peak shock pressure, and crater depth and diameter (Pierazzo et al. 2008). Barr & Citron (2011) showed that 20 CPPR underestimates melt volume by $\sim 15\%$ in simulations of identical projectile and target materials. For our impact configurations, we found 19% and 22% lower melt volume in 20 CPPR simulations compared to 80 CPPR for 30 and 100 km s^{-1} impacts, respectively (Appendix B). Therefore, we multiply the melt volumes in our main analysis by a proportionate correction factor. The time step is limited by the Courant–Friedrichs–Levy criterion, which demands higher temporal resolution for faster material speeds (and impact velocities). We fixed the width of the high-resolution zone, which we found to roughly overlay the inner half of the transient crater. This layout is sufficient for determining melt volume and determining the transient crater diameter (Appendix A). In the literature (e.g., Artemieva & Ivanov 2004), 3D simulations are occasionally used. They are prohibitively expensive for our investigation and unnecessary for exploring quantitative differences in crater profiles resulting from variable impact velocity. We restrict our analysis to head-on, azimuthally symmetric impacts. More information regarding computational methods for impact simulations is discussed by Collins et al. (2012, and references therein).

We focus attention on impacts on the Moon that produce simple craters. Both 2I/Borisov and 'Oumuamua have effective

radii upper bounded by a few hundred meters, and the radii were more likely $\lesssim 100$ m (e.g., Jewitt & Luu 2019), which is insufficient to yield complex craters on the Moon. We assume a target comprised of basalt and projectiles of water ice. We acknowledge that 'Oumuamua was likely not composed of water ice, and that 2I/Borisov was depleted in H_2O. The typical composition of ISOs remains debated, however, and all recent hypotheses have specific, production-limiting aspects (Levine et al. 2021). Nevertheless, 'Oumuamua's anomalous acceleration probably implies a significant volatile component, either in the form of common ices (e.g., H_2O and CO), exotic ices (e.g., H_2, N_2, and CH_4), or a combination of both. We restrict the analysis to a water-ice projectile because (1) the purpose of this study is to investigate whether extremely fast ISO impacts are discernible from those of comets and asteroids, and the main parameter of interest is impact speed; (2) the bulk properties of exotic ices are poorly constrained; and (3) many material properties of H_2O ice are within the same order of magnitude of those of other ices. Nevertheless, an exotic ice projectile composition could affect the crater in a variety of ways. For example, extremely low density H_2 ($\rho \sim 0.08$ g cm^{-3}) would produce a crater of lower volume, owing to a shallower penetration depth $d_b \propto \rho_p^{0.5}$ (Birkhoff et al. 1948). Impacts on Mars are not thoroughly investigated here but would warrant consideration of the planet's thin atmosphere. Exotic ice projectiles would fragment and thus modify the crater morphology (Schultz & Gault 1985). Highly volatile ices may also experience increased ablation at lower velocities, reducing the projectile's mass.

3.2. Simulated Target and Projectile Properties

The material specifications for our simulations are described as follows and listed in Table 1. They are primarily based on parameters used by Prieur et al. (2017) for basalt and Johnson et al. (2016) for water ice. Material strength is set by a Drucker–Prager model, which is most appropriate for granular targets. Required parameters include cohesion Y_0, coefficient of friction f, and limiting strength at high pressure Y_{LIM}. The ϵ–α compaction porosity model (Wünnemann et al. 2006; Collins et al. 2011) is adopted for the target but neglected for the projectile. The required parameters are initial distension $\alpha_0 \equiv 1/(1 - \Phi)$ (for porosity Φ), elastic volumetric strain threshold ϵ_{e0}, transition distension α_X, compaction rate parameter κ, and sound speed ratio χ. Tensile failure remains off, since the target is already assumed to be damaged under the strength model. Acoustic fluidization is neglected, since our simulations only concern simple craters. Dilatancy is also neglected, since it has a very small effect on the transient crater dimensions (Collins 2014). Low-density weakening (a polynomial function of density) and thermal softening (Ohnaka 1995) are enabled.

We proceed to simplify our model by fixing several of the above variables. The porosity parameters are set to $\epsilon_{e0} = 0$, $\alpha_X = 1$, and $\kappa = 0.98$ (Collins et al. 2011), as well as $\chi = 1$ (Wünnemann et al. 2006; Prieur et al. 2017). We fix $f = 0.6$, which is reasonable for sand-like materials. This value was used in early basalt target modeling (Pierazzo et al. 2005), the majority of models in a multilayer lunar cratering study (Prieur et al. 2018), and in more recent impact studies involving basalt targets (e.g., Bowling et al. 2020). The limiting strength Y_{LIM} has a marginal effect on the crater scaling parameters (Prieur et al. 2017); it is fixed to 1 GPa in our simulations. For the water-ice projectile, we fix $Y_0 = 0.01$ MPa, $f = 0.55$, and $Y_{LIM} = 147$ MPa (Johnson et al. 2016).

Table 1
Table of Parameters Used in Our Hydrodynamical Simulations

iSALE Material Parameter	Target	Projectile
Material	Basalt	Ice
EoS type	ANEOS	Tillotson
Poisson ratio	0.25[a]	0.33[b]
Thermal softening constant	1.2[a]	1.84[b]
Melt temperature (K)	1360[a]	273[b]
Simon a parameter (Pa)	$4.5 \times 10^{9,a}$	$6.0 \times 10^{9,c}$
Simon c parameter	3.0[a]	3.0[c]
*Cohesion (damaged) (Pa)	$(5, 1.0 \times 10^7)$	$1.0 \times 10^{4,b}$
Friction coeff. (damaged)	0.6[a]	0.55[b]
Limiting strength (Pa)	$1.0 \times 10^{9,a}$	$1.47 \times 10^{8,b}$
*Initial porosity (%)	(0, 12, 20)	...
Elastic threshold	0.0[a]	...
Transition distension	1.0[a]	...
Compaction rate parameter	0.98[a]	...
Bulk sound speed ratio	1.0[a]	...

Tillotson EoS parameter (ice)	Value
Reference density (g cm^{-3})	0.91[c]
Spec. heat capacity (J kg^{-1} K^{-1})	$2.05 \times 10^{3,c}$
Bulk modulus (Pa)	$9.8 \times 10^{9,c}$
Tillotson B constant (Pa)	$6.5 \times 10^{9,c}$
Tillotson E_0 constant (J kg^{-1})	$1.0 \times 10^{7,c}$
Tillotson a constant	0.3[c]
Tillotson b constant	0.1[c]
Tillotson α constant	10.0[c]
Tillotson β constant	5.0[c]
SIE incipient vaporization (J kg^{-1})	$7.73 \times 10^{5,c}$
SIE complete vaporization (J kg^{-1})	$3.04 \times 10^{6,c}$

Notes. The basalt ANEOS is from Pierazzo et al. (2005). An asterisk denotes parameters varied in our simulations. All fixed parameters include a reference.
[a] Prieur et al. (2017).
[b] Johnson et al. (2016).
[c] Parameter included in the iSALE-Dellen 2D distribution. The ice Tillotson EoS parameters are listed in the bottom section of the table. SIE $\equiv$ specific internal energy.

The remaining material parameters are target Y_0 and Φ. The lunar crust has an average porosity of $\Phi = 12\%$ extending a few kilometers deep (Wieczorek et al. 2013), with variations between 4% and 21%. We perform simulations for three representative values of porosity: $\Phi = 0\%$, 12%, and 20%. We also consider two possibilities for cohesion: $Y_0 = 5$ Pa and $Y_0 = 10$ MPa. The former is representative of granular targets with negligible cohesion (identical to Prieur et al. 2017), while the latter is representative of more competent targets. A cohesion of 10 MPa is the highest cohesion considered by Prieur et al. (2017) and may overestimate the actual cohesion in the heavily fractured and brecciated upper megaregolith, but we adopt 10 MPa for greater contrast against the nearly cohesionless scenario. We use an ANEOS EoS for the basalt and a Tillotson EoS for water ice (parameter values are listed in Table 1).

For each target material combination (Y_0, Φ), we simulated nine impacts spanning projectile diameters $L = 40$, 80, and 160 m and velocities $v_i = 10$, 30, and 100 km s^{-1}. A total of 54 simulations were performed.[2]

---

[2] However, the $\{L = 40$ m, $v_i = 100$ km s^{-1}, $\Phi = 12\%$, $Y_0 = 5$ MPa$\}$ simulation was not numerically stable and is excluded from further analysis.

3.3. Expectations from Late-stage Equivalence

Late-stage equivalence, established by Dienes & Walsh (1970), indicates that information surrounding the projectile is lost in the late stages of crater formation. Indeed, Holsapple & Schmidt (1987) showed that the volume of the resultant crater, for a fixed combination of impactor and target materials, can be estimated by treating the projectile as a point-source characterized by the coupling parameter

$$C = C(L, v_i, \rho_p) = L v_i^\mu \rho_p^\nu. \tag{5}$$

The power-law form follows from the requirements that C remains finite as projectile diameter $L \to 0$, and that C must have fixed dimensionality. The convention adopted by Holsapple & Schmidt (1987) is that C has unity length units. Impacts with equal C produce transient craters with equal volumes. Housen & Holsapple (2011) reviewed constraints on μ and ν from various past experiments. They indicated $\mu \sim 0.55$ for impacts into competent, nonporous rocks, which represents scaling in between momentum and energy dependence. Dry soils have $\mu \sim 0.41$, and highly porous materials are expected to have $\mu < 0.4$. Also, $\nu = 0.4$ has been shown to hold for a variety of materials, even when projectile and target bulk densities differ significantly.

Using Pi-group scaling (Buckingham 1914), one may choose dimensionless parameters,

$$\pi_D \equiv D_{tr} \left(\frac{\rho_t}{m} \right)^{1/3}, \tag{6}$$

$$\pi_2 \equiv \left(\frac{4\pi}{3} \right)^{1/3} \frac{gL}{v_i^2}, \tag{7}$$

$$\pi_3 \equiv \frac{Y}{\rho_t v_i^2}, \tag{8}$$

$$\pi_4 \equiv \frac{\rho_t}{\rho_p} \tag{9}$$

(Holsapple & Schmidt 1982), where D_{tr} is the diameter of the transient crater, and m is the projectile mass. The material strength Y is not precisely defined but relates to cohesion and tensile strength. The transient crater geometry is often used in studies of scaling relations, since it is not dependent on modification (there is also a slight distinction between rim-to-rim dimensions and "apparent" dimensions, which are measured with respect to the preimpact baseline). A properly chosen dimensionless functional relationship $\pi_D = F(\pi_2, \pi_3, \pi_4)$ often serves as a reasonable approximation for crater geometry. Holsapple & Schmidt (1982) provided a general scaling relation,

$$\pi_D = K_1 \left[\pi_2 \pi_4^{\frac{2+\mu-6\nu}{-3\mu}} + (K_2 \pi_3 \pi_4^{\frac{2-6\nu}{-3\mu}})^{\frac{2+\mu}{2}} \right]^{\frac{-\mu}{2+\mu}}, \tag{10}$$

for the empirically determined scaling constants K_1 and K_2 (it is more useful to measure $K_2 Y$ rather than both individual terms). Energy and momentum scaling correspond to $\mu = 2/3$ and $1/3$, respectively, which is readily seen by taking the cube of C. Two regimes are apparent in the above equation: gravity-dominated craters (large π_2 term) and strength-dominated craters (large π_3 term). The former regime is appropriate for craters in the fine-grained lunar regolith, which is of order 10 m

deep (McKay 1991). The lunar megaregolith consists of coarser-grained and heavily brecciated material and extends tens of kilometers deep, and cohesion likely factors into crater formation in this layer. We can use Pi-group scaling to predict which regime our simulations fall into. The transition between regimes occurs roughly when $\pi_2 = (K_2 \pi_3)^{(2+\mu)/2}$, or, equivalently, $(K_2 Y / \rho_t v_i^2)^{1.25} \approx 1.6 gL/v_i^2$, assuming a typical $\mu = 0.5$. Approximating $K_2 Y \approx 20.9 Y_0$ (Prieur et al. 2017) and solving for Y_0, we can find the transition cohesive strength. For example, a 160 m diameter projectile striking at $100 \, \text{km s}^{-1}$ yields ~ 2 MPa. Therefore, our simulations of $Y_0 = 10$ MPa targets are in the strength-dominated regime, whereas those with $Y_0 = 5$ Pa targets are in the gravity-dominated regime. The same holds for other considered projectile diameters and velocities.
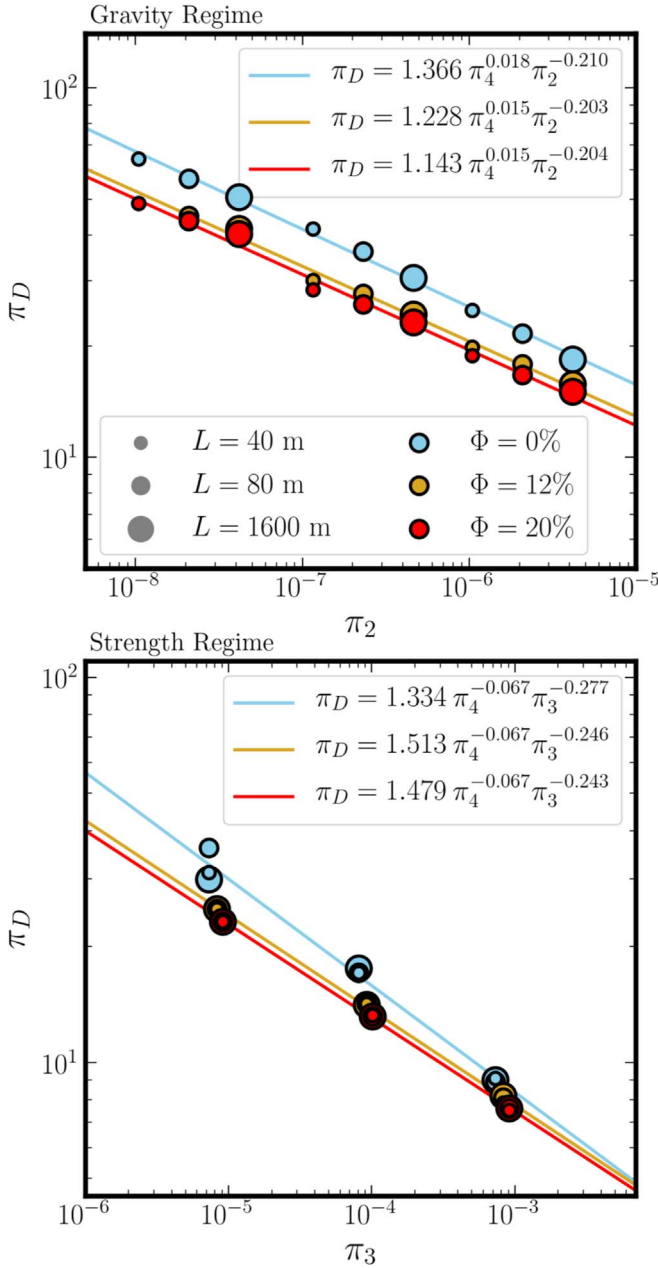
3.4. Results

The simulations closely follow trends consistent with late-stage equivalence: power-law functions of the dimensionless Pi-group scaling parameters. The results are shown in Figure 2 for both the gravity- and strength-dominated regimes. In the former case, we fit a power law between π_D and π_2, and in the latter case, we fit a power law between π_D and π_3; subsequently, we solve for μ. Outcomes for the three target porosities/distentions were fit separately, since they represent distinct target materials. In the gravity-dominated regime, we find $\mu = (0.533, 0.510, 0.514)$ for $\Phi = (0\%, 12\%, 20\%)$ scenarios. In the strength-dominated regime, we find $\mu = (0.554, 0.493, 0.486)$. Across all fits, the maximum deviation of π_D from a power-law fit is 7%. Discrepancies are addressed in Section 5, but the overall conformity of the dimensionless scaling parameters to a power-law relationship confirms subenergy scaling of the crater diameter for projectile speeds up to $100 \, \text{km s}^{-1}$.

In order to highlight the difficulty of inferring projectile characteristics from transient crater diameter alone, snapshots of two simulations are shown in Figure 3. One represents a slow, large projectile, whereas the other represents a fast, small projectile impacting the same target material. Both simulations involved negligible target cohesive strength. Their transient diameters differ by $\sim 1\%$. The diameters are "apparent" (i.e., measured at the level of the preimpact surface). There are slight differences in their (transient) profiles and depths; however, we do not explore these aspects in detail, since they will largely change in the subsequent modification stage. Figure 3 also shows contours of peak shock pressure, which may be used to infer melt volume. This point is investigated in Section 4.

4. Impact Melt Volume

As discussed above, there are well-known degeneracies between projectile mass, velocity, and impact angle in forming a crater. However, combinations of scaling relationships offer an opportunity to isolate variables of interest. Melt production is of particular interest because it generally does not scale according to the point-source limit (Pierazzo et al. 1997). As a relatively recent example, Silber et al. (2018) simulated impacts of dunite projectiles into the Moon with v_i ranging from 6 to $20 \, \text{km s}^{-1}$. They found a difference of 2 orders of magnitude in melt volume in craters with equal diameter, which shows the potential of using crater observables to deduce impact velocity. In our investigation of scaling relations, we restrict the analysis to vertical impacts and neglect the dependence on impact angle.

Figure 2. Dimensionless scaling parameter outcomes for the iSALE simulations. Results for gravity-dominated craters are shown in the top panel, whereas those for strength-dominated craters are in the bottom panel. Colors denote three different target porosities, and the sizes of the data points are proportional to the projectile diameter. The best-fit power-law equations are denoted in the top right corner of each panel.

4.1. Numerical Simulations of Melt Production

Melt volume in numerical simulations may be estimated by recording the peak shock pressure experienced by Lagrangian tracer particles (e.g., Wünnemann et al. 2008). Plastic deformation from the shock wave irreversibly heats the target. If the target is shocked to a sufficient pressure, it lies above the melt temperature following isentropic release from the rarefaction wave. A critical shock pressure for complete melting $P_c = 106$ GPa is adopted for basalt (Quintana et al. 2015).

The bottom panels of Figure 3 show the peak shock pressures experienced in two representative examples of our hydro simulations as a function of initial location in the target.

The faster impact generates significantly higher peak pressures overall. In our presentation of results, we combine melt and vapor into a single "melt" volume wherever peak shock pressures exceed P_c. Per Appendix B, all melt volumes were scaled by a correction factor to account for the simulation resolution of 20 CPPR. Melt volumes from all simulations are listed in the last column of Table 2. Some immediately recognizable trends include the following: the melt volume spans approximately 3 orders of magnitude, where the greatest melt volumes arise from the largest, fastest projectiles; only 30 and 100 km s^{-1} impacts generated nontrivial melt volumes; holding other variables constant, target cohesion affects melt volume at a $\lesssim 10\%$ level in our simulations; and zero porosity yields ~20% greater melt volume than the most porous materials explored.

Can enhanced melt volumes assist in identifying the highest-speed impacts? The presence of significant basaltic melt can immediately rule out $\leqslant 10$ km s^{-1} impacts. However, at a constant D_{tr}, melt volume differences between 30 and 100 km s^{-1} impacts are more subtle. For example, 100 km s^{-1} impacts of 40 m projectiles produce similar D_{tr} and melt volumes as 30 km s^{-1} impacts of 80 m projectiles. Figure 3 depicts this comparison for two example simulations. Note that the larger, slower projectile does yield a larger transient crater diameter and less melt; however, if actual lunar craters exhibit these properties, the differences between these two cases are probably too small to differentiate. Therefore, melt volume may be an important metric for filtering out low-speed asteroid impacts but is less useful at the high-speed tail of the impact speed distribution for these specific combinations of projectile and target materials. We proceed to place the simulation results in the context of established scaling relations.

4.2. Scaling Relations of Crater Dimensions and Melt Volume

Pierazzo et al. (1997) performed hydrocode simulations of impacts with various materials and fit a power law of the form

$$\log\left(\frac{V_M}{V_p}\right) = a + \frac{3}{2}\mu' \log\left(\frac{v_i^2}{E_M}\right), \quad (11)$$

a relation originally considered by Bjorkman & Holsapple (1987). In the above, $a = \log k$, where k is a constant of proportionality that arises because the equation is based on dimensional analysis, V_p denotes the projectile volume, V_M denotes the melt volume, μ' is a scaling constant, and E_M is the specific energy of melting. Values of E_M for several materials of interest are listed by Bjorkman & Holsapple (1987) and Pierazzo et al. (1997), as well as Quintana et al. (2015) for basalt.

In general, $\mu \neq \mu'$ because the transient crater diameter scales according to the point-source limit, whereas melt volume does not. Indeed, Okeefe & Ahrens (1977) and Pierazzo et al. (1997) suggested that μ' is consistent with $2/3$ (energy scaling). More recent works (Barr & Citron 2011; Quintana et al. 2015) reaffirm energy scaling for melt numbers $v_i^2/E_M \gtrsim 30$. Meanwhile, $\mu < 2/3$ for many materials of interest (Schmidt & Housen 1987). In an ideal situation and holding all other variables constant, combined measurements of crater diameter and melt volume can, in theory, break the degeneracy between projectile mass and velocity. This premise is elaborated upon in Appendix C, where we derive equations for melt volume as a function of impact velocity and transient
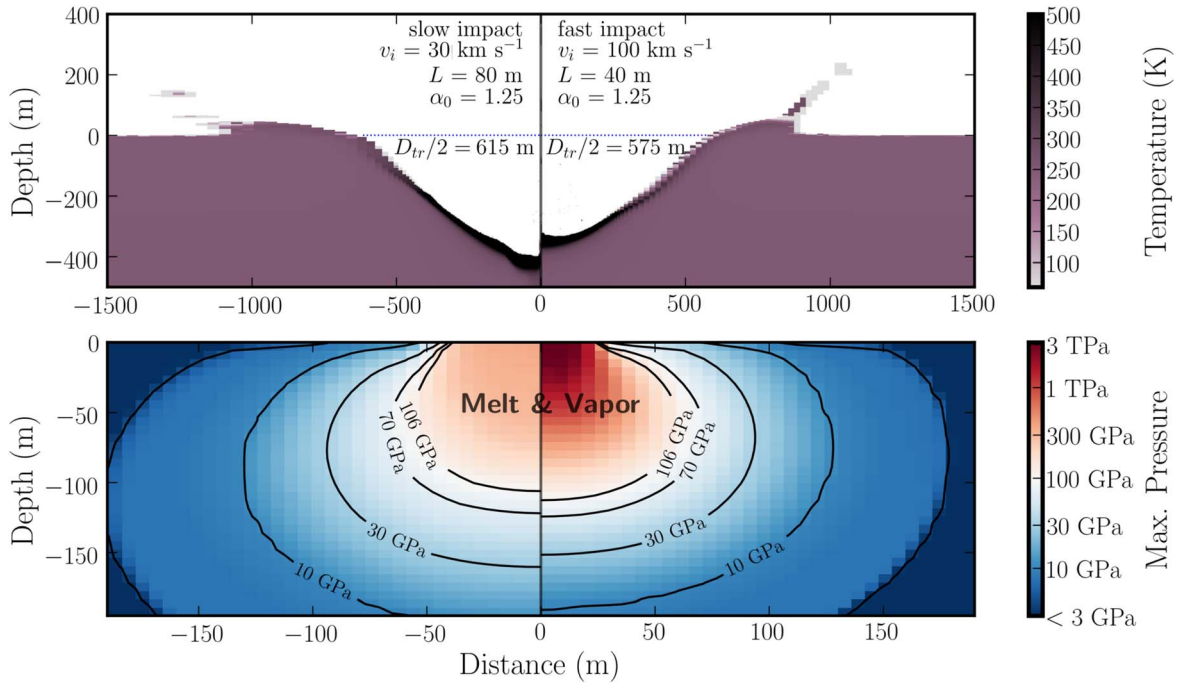
Figure 3. Two example simulations of ice projectiles impacting into a basalt target, shown to highlight similarities in transient craters under different impact conditions. The left panels correspond to a slow impact (30 km s^{-1}) and large projectile diameter (80 m), and the right panels correspond to a fast impact (100 km s^{-1}) and small projectile diameter (40 m). The simulated targets have identical initial target distensions (α_0) and negligible cohesive strength. The top panels depict the transient crater profiles. The reported transient radii ($D_{tr}/2$) are measured relative to the preimpact surface. The bottom panels depict the peak shock pressures experienced by tracer particles, which were embedded in the high-resolution zone. The contours are derived from the initial position tracer particles. The critical shock pressure for complete melting is $P_c = 106$ GPa. Note the different abscissa and ordinate scales between the top and bottom panels.

crater diameter and demonstrate

$$V_M \propto D_{\mathrm{tr}}^x v_i^{3(\mu'-\mu)} \qquad (12)$$

for sufficiently fast impacts. The constant of proportionality depends on the materials involved. In the strength-dominated regime, $x = 3$, and in the gravity-dominated regime, $x = (6 + 3\mu)/2$. This relationship is independent of m and L, so one may, in principle, solve for v_i from two crater measurements. In practice, the impact angle, target lithology, and variable composition of ISOs and other projectiles add degeneracies that would significantly complicate efforts to find an ISO crater. Additionally, long-term modification processes may alter crater morphology and make inferences of D_{tr} less accurate. However, our exploration is designed to gauge the baseline feasibility of crater identification using these two observables, which may serve as a starting point for more sophisticated models that employ other sources of data (e.g., those discussed in Section 5).

As follows, we make a theoretical quantification of melt volume and draw comparisons to our hydro simulations. The analysis requires determining the constant of proportionality in Equation (12), which depends nontrivially on material properties including the coefficient of friction, porosity, and cohesive strength, in addition to impact angle (Schmidt & Housen 1987; Elbeshausen et al. 2009; Prieur et al. 2017). We take Equations (C4) and (C7) to analytically describe melt production in the gravity- and strength-dominated regimes, respectively, and rearrange to obtain a function for impact velocity. We adopt a melt energy $E_M = 8.7 \times 10^6$ J kg^{-1} for the basalt target (Quintana et al. 2015) with density $\rho_t = 2.86$ g cm^{-3} (modified accordingly for nonzero porosity); a water-ice projectile is assumed with $\rho_p = 0.91$ g cm^{-3}. In all cases, we assume $\nu = 0.4$ and $g = 1.62$ m s^{-1}. The empirical parameter K_1 was measured for each target material in Section 3 and is typically of order unity (Prieur et al. 2017). Finally, we find that $a = -0.890$ and $\mu' = 0.535$ reasonably describe all melt volume outcomes from our simulations (see Section 5 for details). In this manner, we may investigate whether the simulation results agree with the theoretical scaling relations for melt volume. Further, we may use the scaling relations to extend our analysis to a broader range of materials than those simulated and investigate the conditions most amenable to crater identification.

The relationship between D_{tr}, V_M, and v_i is plotted in Figure 4 for targets with $\Phi = 20\%$ in the gravity-dominated regime. The 10 km s^{-1} impacts are excluded, since the melt number is less than 30; the cutoff is at approximately 16 km s^{-1}. We plot contour lines for 16 km s^{-1}, as well 30 and 100 km s^{-1}. The difference between the diameter scaling exponent μ and the melt volume scaling exponent μ' determines the velocity spread across D_{tr} and V_M. Increasingly significant velocity dependence manifests as a more gradual gradient in the figure and larger separation between constant velocity lines. The results in Figure 4 are representative of the other porosities in that $\mu \simeq \mu'$, so the distance between velocity contours is small. This trend indicates that melt volume may not be a significantly differentiating metric for inferring projectile parameters, at least for the materials simulated here.

Nevertheless, other impact configurations may be more conducive for breaking degeneracy with combined D_{tr} and V_M measurements. The parameterization $a = -0.482$ and $\mu' = 0.624$ (Barr & Citron 2011) is suitable for impacts of identical target and projectile materials (spanning aluminum, iron, ice, dunite, and granite). We calculated the melt volume for several parameter combinations that span the various
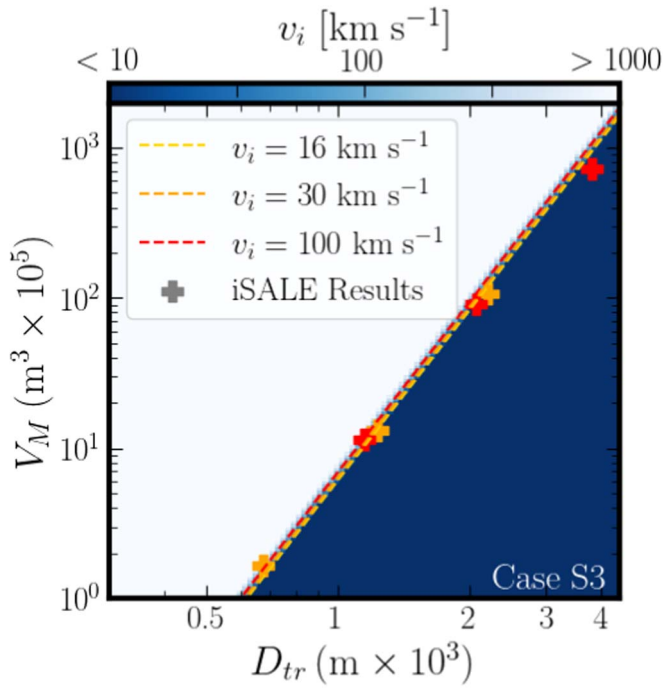
Table 2
Summary of Hydrodynamic Simulations

L (m)	v_i (km s^{-1})	Y_0 (Pa)	ρ_t^{ref} (g cm^{-3})	ρ_p (g cm^{-3})	Φ (%)	D_{tr} (km)	V_M^* (m$^3 \times 10^5$)
40	10	5	2.86	0.91	0	0.55	0
40	10	5	2.86	0.91	12	0.46	0
40	10	5	2.86	0.91	20	0.45	0
40	10	1×10^7	2.86	0.91	0	0.20	0
40	10	1×10^7	2.86	0.91	12	0.18	0
40	10	1×10^7	2.86	0.91	20	0.01	0
40	30	5	2.86	0.91	0	0.91	1.95
40	30	5	2.86	0.91	12	0.69	1.76
40	30	5	2.86	0.91	20	0.67	1.66
40	30	1×10^7	2.86	0.91	0	0.38	1.95
40	30	1×10^7	2.86	0.91	12	0.33	1.76
40	30	1×10^7	2.86	0.91	20	0.31	1.66
40	100	5	2.86	0.91	0	1.41	13.61
40	100	5	2.86	0.91	20	1.15	11.45
40	100	1×10^7	2.86	0.91	0	0.95	13.59
40	100	1×10^7	2.86	0.91	12	0.57	12.13
40	100	1×10^7	2.86	0.91	20	0.55	11.44
80	10	5	2.86	0.91	0	0.95	0
80	10	5	2.86	0.91	12	0.45	0
80	10	5	2.86	0.91	20	0.79	0
80	10	1×10^7	2.86	0.91	0	0.39	0
80	10	1×10^7	2.86	0.91	12	0.37	0
80	10	1×10^7	2.86	0.91	20	0.36	0
80	30	5	2.86	0.91	0	1.59	15.55
80	30	5	2.86	0.91	12	1.27	14.08
80	30	5	2.86	0.91	20	1.23	13.29
80	30	1×10^7	2.86	0.91	0	0.75	15.63
80	30	1×10^7	2.86	0.91	12	0.65	14.07
80	30	1×10^7	2.86	0.91	20	0.62	13.31
80	100	5	2.86	0.91	0	2.50	108.87
80	100	5	2.86	0.91	12	2.07	96.84
80	100	5	2.86	0.91	20	2.07	91.08
80	100	1×10^7	2.86	0.91	0	1.59	108.78
80	100	1×10^7	2.86	0.91	12	1.15	96.78
80	100	1×10^7	2.86	0.91	20	1.10	91.35
160	10	5	2.86	0.91	0	1.62	0
160	10	5	2.86	0.91	12	1.45	0
160	10	5	2.86	0.91	20	1.43	0
160	10	1×10^7	2.86	0.91	0	0.79	0
160	10	1×10^7	2.86	0.91	12	0.75	0
160	10	1×10^7	2.86	0.91	20	0.72	0
160	30	5	2.86	0.91	0	2.69	124.35
160	30	5	2.86	0.91	12	2.24	112.85
160	30	5	2.86	0.91	20	2.20	106.49
160	30	1×10^7	2.86	0.91	0	1.54	124.73
160	30	1×10^7	2.86	0.91	12	1.30	112.44
160	30	1×10^7	2.86	0.91	20	1.25	106.43
160	100	5	2.86	0.91	0	4.45	869.22
160	100	5	2.86	0.91	12	3.81	773.89
160	100	5	2.86	0.91	20	3.81	729.39
160	100	1×10^7	2.86	0.91	0	3.49	870.34
160	100	1×10^7	2.86	0.91	12	3.01	772.02
160	100	1×10^7	2.86	0.91	20	2.20	732.64

Note. Parameters left of the divider denote, from left to right, projectile diameter, impact speed, target cohesive strength, target reference density (i.e., notwithstanding porosity), projectile density, and porosity. Measured quantities right of the divider are transient crater diameter and melt volume. *The reported melt volume is higher than the simulation output owing to a correction (23%–28% increase) that accounts for spatial resolution (Appendix B).

regimes covered in prior studies as follows. The specific combinations are listed in Table 3. The parameters from Schmidt & Housen (1987) are empirical, where wet and dry sand were used as proxies for competent and porous rock, respectively. The iSALE-2D simulations by Prieur et al. (2017) assumed a basalt target with a variable coefficient of friction (f) and porosity (Φ). Elbeshausen et al. (2009) simulated oblique impacts into granite with iSALE-3D, varying f and θ with fixed $\Phi = 0\%$. Since their coefficients are reported in terms of volume scaling (π_V), we do not consider specific instances of their simulations. They find $\mu \simeq 0.469$ for $f = 0.7$ and $\mu = 0.548$ for $f = 0.0$, which are comparable to some

Figure 4. Analytic estimates of impact speed as a function of the melt volume and diameter of the transient crater for case S3 (see Table 3). The relationship between the three variables follows from scaling relations. Scaling parameters were fit using the simulated transient diameters and melt volumes. For reference, isovelocity contours are plotted for 16 (at which point the scaling relation becomes valid and is also characteristic of asteroid impacts), 30, and 100 km s^{-1}, and the simulation results for 30 and 100 km s^{-1} impacts are marked.

scenarios from Schmidt & Housen (1987) and Prieur et al. (2017).

Impacts involving dry sand or porous basalt have the lowest values of μ, and the melt volume for $v_i = 16$–100 km s^{-1} spans approximately 0.5 dex at a fixed transient crater diameter (Figure 5). In contrast to porous scenarios, wet sand results in the least spread, making it the most challenging for identifying ISO impact craters. We emphasize the critical importance that melt approximately scales with energy for these materials; otherwise, velocity dependence effectively vanishes (Abramov et al. 2012). The results are encouraging for lunar melts that involve the unconsolidated regolith (McKay 1991) and lunar crust of porosity $\Phi \sim 10\%$–20% (Kiefer et al. 2012). In practice, μ and K_1 would both require tight constraints and hence depend on whether the crater in question formed in the basaltic mare or anorthosite highlands. Additional considerations include impact angle and projectile density.

5. Discussion and Conclusions

Intensive study of the lunar cratering record, including prospects for identifying ISO craters, will soon be forthcoming. The year 2020 marked the first lunar sample return mission in nearly 45 yr by the Chang'e 5 Lander (Zeng et al. 2017); this is a precursor to a modern-day surge in lunar exploration, as well as preliminary steps to establishing a permanent presence on Mars. We discuss how upcoming remote observations, return missions, and in situ analyses might assist in the identification of ISO impact craters.

5.1. Measuring Melt Volumes in Search of ISO Craters

In the previous section, we showed that a high-speed ISO impact can yield a significantly enhanced melt volume for certain projectile/target material combinations. While other factors need to be accounted for, including impact angle and target material properties, melt volume can help break the degeneracy between impact velocity and projectile mass, specifically, by searching for craters that fall in the high melt volume, low-diameter regime. In situ analyses (e.g., Grieve & Cintala 1982) combine the percentage of melt in localized regions with crater geometry to obtain an overall estimate of melt volume. However, there are significant sources of uncertainty (French 1998), such as a strong dependence on target materials (e.g volatile content; Kieffer & Simonds 1980) and modification processes (Melosh 1989). Furthermore, detailed mapping of large melt volumes may be forbiddingly time- and resource-intensive for surveying candidate ISO craters, given there should be only of order unity high-speed ISO impact craters between the Moon and Mars (Section 2).

Remote sensing melt volume may be an appealing alternative to in situ analyses. Currently, some of the best remote-based estimates rely on LROC images (Plescia et al. 2014), where melt pools are identifiable by low-albedo, flat crater floors. Crater diameters may also be readily extracted from LROC images. The correspondence between final and transient crater diameters is nontrivial; however, a simple heuristic would be to search for craters with particularly high ratios of melt volume to diameter as potentially of ISO origin. Plescia et al. (2014) estimated the melt volume by fitting the crater wall profile, extrapolating the profile to depths below the melt pool, and taking the difference between the observed crater volume and that of the entire original crater. They acknowledge that the estimates are order-of-magnitude, since additional melt may have been ejected from the crater, displaced onto the crater wall, or buried within the debris layer on the crater floor. Silber et al. (2018) analyzed theoretical (from iSALE-2D) and observed (Plescia et al. 2014) melt volumes of lunar craters, with a similar goal as ours of breaking degeneracies between projectile characteristics. They were able to match the observed spread in melt volume ($\sim$2 orders of magnitude) for a given crater diameter. Individual craters/projectiles were not investigated, and velocities only up to 20 km s^{-1} were considered. These results indicate that imaging may be a viable method of finding enhanced melt volumes; however, given that remote sensing uncertainties are of the same order as the largest melt volume spreads for a fixed D_{tr} (see Section 4), higher-precision follow-up measurements may be necessary, possibly in situ.

The precision in melt volume required to identify an ISO crater depends on the target materials, apparent in the variable spread in Figure 5. Lunar seismology (e.g., of small impacts) may soon be a feasible approach for estimating melt volumes without requiring assumptions of the subsurface crater geometry. The arrival time anomalies of p and s waves are frequently used to map geological structures such as mantle plumes (Nataf 2000) and are also employed for identifying and characterizing natural oil reserves. For our purposes, we note that simple craters tend to have a "breccia lens" at their floors, which is a mixture of inclusion-poor breccia that formed immediately below the impact and mixed breccia that formed due to the shear of melt sliding up the crater walls (this material collapsed during the modification stage; Grieve 1987).

Table 3
Parameter Combinations for Analytically Linking Melt Volume, Transient Crater Diameter, and Impact Velocity

Case	a	μ'	K_1	μ	Case Description
S1	−0.890	0.535	1.366	0.533	Ice projectile, basalt target, $Y = 5$ Pa, $\Phi = 0\%$ (this study)
S2	−0.890	0.535	1.228	0.510	Ice projectile, basalt target, $Y = 5$ Pa, $\Phi = 12\%$ (this study)
S3	−0.890	0.535	1.143	0.514	Ice projectile, basalt target, $Y = 5$ Pa, $\Phi = 20\%$ (this study)
S4	−0.890	0.535	1.334	0.554	Ice projectile, basalt target, $Y = 10^7$ Pa, $\Phi = 0\%$ (this study)
S5	−0.890	0.535	1.513	0.493	Ice projectile, basalt target, $Y = 10^7$ Pa, $\Phi = 12\%$ (this study)
S6	−0.890	0.535	1.479	0.486	Ice projectile, basalt target, $Y = 10^7$ Pa, $\Phi = 20\%$ (this study)
E1	−0.482[a]	0.624[a]	1.6	0.564	Wet sand (proxy for competent rock; Schmidt & Housen 1987)
E2	−0.482[a]	0.624[a]	1.4	0.381	Dry quartz sand (proxy for porous rock; Schmidt & Housen 1987)
E3	−0.482[a]	0.624[a]	1.615	0.558	Basalt, wet sand analog, $f = 0.1$, $\Phi = 0\%$ (Prieur et al. 2017)
E4	−0.482[a]	0.624[a]	1.585	0.516	Basalt, porous sand analog, $f = 0.1$, $\Phi = 12\%$ (Prieur et al. 2017)
E5	−0.482[a]	0.624[a]	1.984	0.394	Basalt, porous sand analog, $f = 0.6$, $\Phi = 12\%$ (Prieur et al. 2017)
E6	−0.482[a]	0.624[a]	1.473	0.424	Basalt, porous sand analog, $f = 0.6$, $\Phi = 40\%$ (Prieur et al. 2017)

Notes. Columns correspond to case number (S denotes simulated, E denotes extended), melt volume scaling constant and exponent (a and μ'), transient crater diameter scaling coefficient (K_1), crater diameter scaling exponent (μ), and a brief description of the case study. The combinations of parameters are derived from our simulations in the top portion and sample different regimes reported by Schmidt & Housen (1987) and Prieur et al. (2017) in the bottom portion. For specific scenarios from Prieur et al. (2017), f denotes coefficient of friction, and Φ denotes porosity.
[a] For case studies not simulated in this study, we adopt identical a and μ' from Barr & Citron (2011), which was found to hold for a variety of materials.

Appropriately placed sensors within and near an existing crater may allow seismic imaging of the breccia lens if the recrystallized melt has sufficiently different material properties from surrounding rock or there is a discontinuity in wave propagation between the crater wall and the breccia lens. Seismic imaging of artificial shots/blasts has been applied extensively to the Chicxulub crater (Gulick et al. 2013), for example, in identification of the top of its melt sheet (Barton et al. 2010). It was also used to measure melt volume in the Sudbury Basin (Wu et al. 1995). Seismic imaging could, in principle, extend to the Moon for measuring melt volume, although it is still subject to uncertainties surrounding ejected or displaced melt during the crater's formation.

5.2. Petrological Considerations

In addition to producing more melt, faster impacts induce higher peak shock pressures. We discuss whether high-pressure petrology provides an alternative or complementary route to identifying ISO impact craters.

Target material in our 100 km s^{-1} simulations experienced higher peak pressures ($\sim$3 TPa) compared to target material in the 30 km s^{-1} simulations (Figure 3). In both cases, the pressures are sufficiently high to produce coesite, stishovite, and maskelynite (Stöeffler 1972; Melosh 2007), so high-pressure phases and polymorphs are probably insufficient criteria for identifying an ISO crater. However, the abundance or composition of vapor condensates might point to an ISO projectile. To date, only a handful of lunar vapor condensates have ever been found (Keller & McKay 1992; Warren 2008). High-alumina silica-poor (HASP) material (Naney et al. 1976) deemed evaporation residue is complemented by volatile-rich alumina-poor (VRAP) glasses and gas-associated spheroidal precipitates (GASP). These spheres are attributed to liquid condensation droplets (VRAP is enriched in volatiles like K_2O and Na_2O, whereas GASP is not; VRAP spheres are also about 200–400 nm in diameter, whereas GASP spheres span roughly 2–10 μm). The VRAP/GASP are identified by a distinct depletion of refractory species Al_2O_3 and CaO. The highest-speed impacts (e.g., ISOs) may generate more vapor condensates, which may be detected in surrounding rock

samples. Also, the exceptionally high pressures generated in ISO impacts may alter the composition of residues and condensates; for example, pressures may be sufficient to shock vaporize Al_2O_3, CaO, or TiO_2, depleting them from HASP and enhancing them in condensates. Predicting the constituents of vapor condensates associated with ISO impacts will require mapping the high-pressure phase space for low-volatility target materials.

Microscopic spherules were also produced through ancient lunar volcanism (Reid et al. 1973), but these spherules can be robustly distinguished from those of impact origin. Warren (2008) used a combination of Al content, as well as trends of TiO_2 and MgO, to establish an impact origin. As another example, Levine et al. (2005) ruled out a volcanic origin for >90% of 81 spherules in an Apollo 12 soil sample based on low Mg/Al weight ratios. They also found that a large fraction had $^{40}Ar/^{39}Ar$ isochron ages younger than 500 Myr, which is inconsistent with known periods of lunar volcanism.

Impact speed also influences the dimensions of vapor condensates. Johnson & Melosh (2012a) presented a model for the condensation of spherules from impact-generated rock vapor. They found that the highest impact speeds yield smaller spherule diameters owing to higher-speed expansion of the vapor plume for impact speeds greater than $\sim$28 km s^{-1}. The vapor plume model of Johnson & Melosh (2012a) invokes a simplified plume geometry and assumes that the projectile and target are both comprised of SiO_2. The same authors employed this model when they estimated projectile velocities and diameters for major impact events in Earth's history (Johnson & Melosh 2012b). In theory, particularly small spherules may be linked to impact speeds consistent with ISOs. Johnson & Melosh (2012a) explored velocities up to 50 km s^{-1}, but extrapolation suggests that 100 km s^{-1} impacts may produce spherules of diameter $\lesssim 10^{-7}$ m. Degeneracy with projectile size persists but might be reconciled with, for example, crater scaling relationships. In regard to identifying ISO craters on the Moon, a significant concern is that vapor condensate spherules may be scattered extremely far from the impact site. For example, microkrystite condensates from the K-T impact form a worldwide spherule layer (Smit et al. 1992). Isolating the crater of origin would likely require widespread mapping and
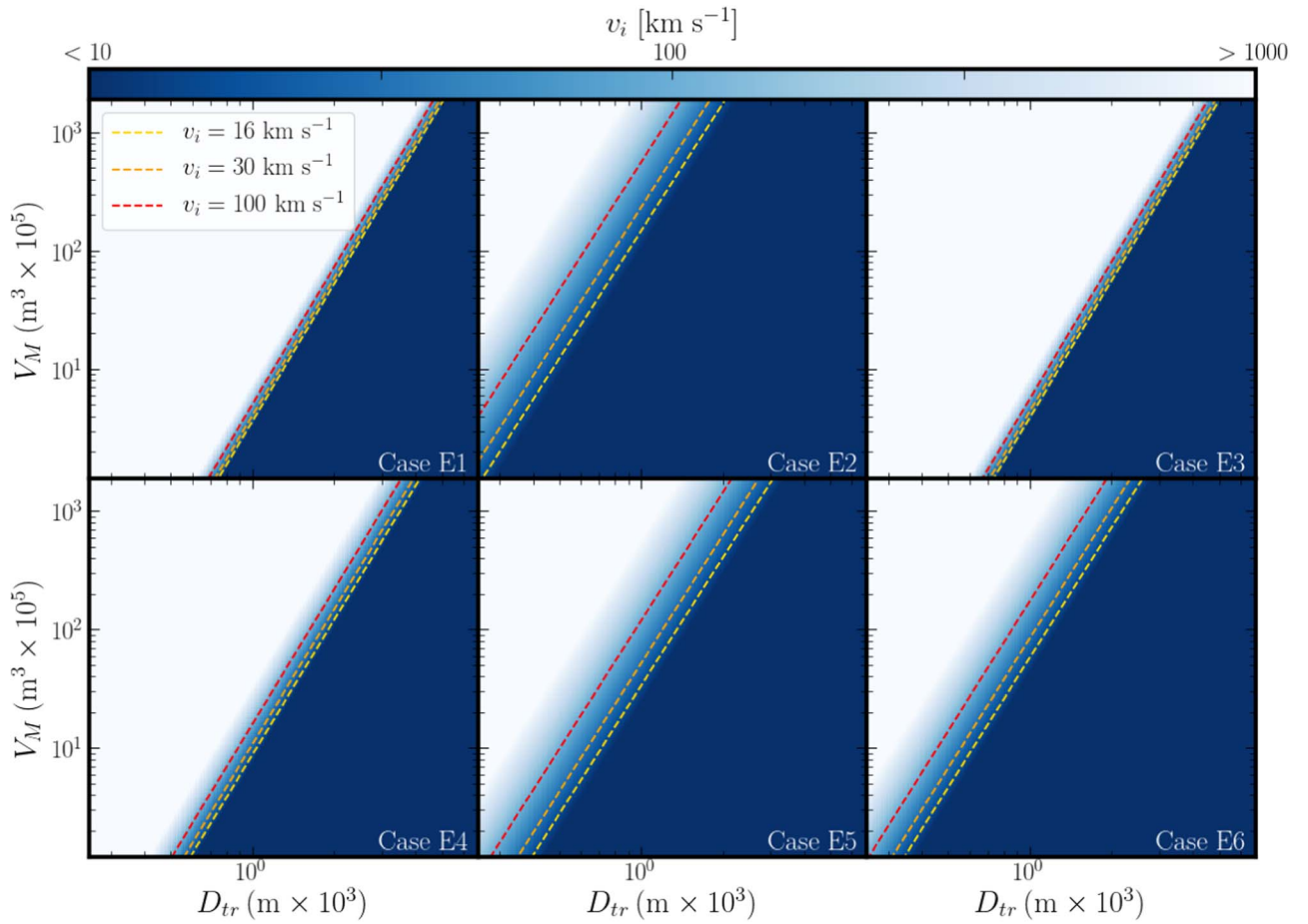
Figure 5. Analytic estimates of impact speed as a function of melt volume and diameter of the transient crater for six examples of target materials that are explored theoretically without dedicated simulations in this study. The panels show predictions for impacts into targets with various scaling parameterizations (representing different materials), which are listed in Table 3. Lines of constant impact velocity are drawn for 16, 30, and 100 km s^{-1}, denoted by varying line colors. The larger the separation between these lines, the greater the difference in melt volume produced in craters of the same diameter, and hence the easier to determine projectile characteristics.

classification of spherules on the Moon, which is beyond current capabilities.

Could melts or condensates be used to infer an ISO's composition? It is well understood that these impact products comprise a mixture of projectile and target material. For example, Smit et al. (1992) estimated that condensate spherules from the K-T impact contain an ∼10% bolide component from their Ir content. However, the task might be challenging for lunar vapor condensates because the spherules are microscopic and of extremely low abundance in the Moon's crust (<0.001% by volume; Warren et al. 2008). Keller & McKay (1992) and Warren (2008) do not make inferences regarding the composition of the projectile(s) that generated the VRAP/GASP spherules, and to our knowledge, there has not yet been any study that links these spherules or the HASP residue to a projectile's composition.

Encouragingly, a number of projectiles involved in terrestrial impacts have been geochemically characterized, primarily via rocks within and near the crater. Tagle & Hecht (2006) reviewed the major findings and methods. Elemental ratios of PGEs (Os, Ir, Ru, Pt, Rh, and Pd), plus Ni and Cr, are particularly effective if multiple impactite samples are available, since it is not then necessary to correct for elemental abundances in the target. Isotope ratios ^{53}Cr/^{52}Cr and ^{187}Os/^{188}Os are also commonly employed. This precedent extends to lunar impacts, as Tagle (2005) used PGE ratios in Apollo 17 samples to determine that the

Serenitatis Basin projectile was an LL-ordinary chondrite. Since these methods are based on refractory species, ISOs may be difficult to characterize. Comet 2I/Borisov contains a significant volatile component (Bodewits et al. 2020), as most comets do, and volatiles would explain 'Oumuamua's anomalous acceleration (Seligman et al. 2019). If ISOs have a refractory component, then elemental and isotopic ratios could separate them from other projectile classes and offer important insights into their composition.

5.3. Influence of Impact Angle

Crater dimensions are degenerate with impact angle, a parameter unexplored in this study. Indeed, the most probable impact angle of 45° would yield a considerably different crater than a head-on collision, all other factors being equal. Davison et al. (2011) quantified how several crater properties depend on impact angle. For example, crater volume is approximately halved for a 45° impact, but the crater remains symmetrical for impact angles θ greater than a threshold $\theta_e \sim 10°–30°$, depending on the target material. They also found crater depth scales with $\sin \theta$ and width with $\sin^{0.46} \theta$. Melt production exhibits a strong dependence on impact angle, as shown by Pierazzo & Melosh (2000) through simulations of Chicxulub-type impacts. In their 20 km s^{-1} impact speed simulations, the volume of material shocked above 100 GPa at $\theta = 30°$ was roughly half that of a head-on collision and trivial

for $\theta < 15°$. While melt volume scales with impact energy (Bjorkman & Holsapple [1987]), the scaling breaks down if only the vertical component is considered in oblique impacts (i.e., $(v_i \sin \theta)^2$; Pierazzo & Melosh [2000]). Nevertheless, melt volume was found to be proportional to transient crater volume across variations in θ, with oblique impacts producing asymmetric melts.

How crater properties change with joint variations in impact angle and speed, especially in the $v_i > 100$ km s^{-1} regime, would be interesting for future investigation, albeit computationally expensive. The studies discussed above indicate that crater and melt asymmetries may prove useful for constraining the angle of incidence. They also suggest that the maximal pressures and melt volumes produced by real ISO impacts are probably lower than those attained in our simulations, and that the real crater dimensions may exhibit different ratios than those of our simulated craters. The reduction in peak shock pressure may also eliminate certain petrological indicators of a high-speed impact, such as vapor condensates.

5.4. Analysis of Scaling Exponents

In Section [3], we fit power-law relationships to dimensionless parameters (Equations ([6])–([9])) to determine the transient diameter scaling exponent μ. An accurate and precise μ is needed in order to gauge the efficacy of using melt volume to disentangle projectile properties (Section [4]). Inspection of the top panel of Figure [2] (gravity regime) shows that data points for fixed velocity follow a local slope that deviates slightly from the global fitted slope. This effect is especially pronounced for the two porous scenarios. For example, in the $\Phi = 20\%$ simulations, locally fitting a power law to outcomes of simulations with a fixed projectile velocity yield μ ranging from 0.32 to 0.38 (increasing with decreasing impact velocity). This discrepancy from the global fit $\mu = 0.514$ may arise from an additional velocity dependence that is not incorporated into the Pi-group scaling framework. A similar anomaly was reported by Prieur et al. ([2017]) when comparing their results to those of Wünnemann et al. ([2011]). Discrepancies in π_D reached up to 10% between the two sets of simulations, which were conducted at 12.7 and 5 km s^{-1}, respectively. The premise that μ may depend on impact velocity has been noted before. For example, Yamamoto et al. ([2017]) found a dependence even when the impact velocity greatly exceeds the target bulk sound speed. Their interpretation is that the dependency arises because the shock front pressure decays at a rate q, which itself depends on impact velocity. This dependency suggests that it may be necessary to run a grid of simulations, densely spanning L and v_i for a fixed target composition, in order to constrain the allowed values for μ.

We also comment on the melt volume scaling parameters a and μ' in Equation ([11]). Barr & Citron ([2011]) performed simulations of impacts involving identical projectile and target materials and fit all outcomes simultaneously to obtain $a = -0.482$ and $\mu' = 0.624$. Their simulations of an ice projectile striking dunite, which is the most similar scenario to our simulations, yielded $a = -1.78$ and $\mu' = 0.819$. This value for μ' is unexpectedly high, since it exceeds the theoretical upper bound of energy scaling. We attempted to independently determine these two parameters from melt volumes in our simulations. The 10 km s^{-1} impact velocity scenarios were excluded. While our fit involves only two velocities, all of the materials considered produce similar melt volumes for a given L and v_i. Fitting all simulation outcomes simultaneously yielded $a = -0.890$ and $\mu' = 0.535$. The scaling exponent is considerably lower that that found by Barr & Citron ([2011]). It is

closer to the $\mu' = 0.432$ found by Pierazzo et al. ([1997]) for ice/ice impacts (although Barr & Citron [2011] suggested that this value was influenced by the choice of target temperature by Pierazzo et al. [1997]). The discrepancy between our result and that of Barr & Citron ([2011]) could arise from our choice of basalt as a target material or differences in the adopted EoS (Tillotson versus ANEOS). We also evaluated μ' using the 80 CPPR simulations from Appendix [C] to make the fit robust against our melt volume correction scheme; however, we obtained a comparable $\mu' = 0.564$. To investigate μ' further, we ran additional 20 and 50 km s^{-1} impact simulations for one configuration involving a cohesionless, porous target. Fitting all velocities (20, 30, 50, and 100 km s^{-1}) yielded $\mu' = 0.584$, while fitting just the lowest two velocities yielded $\mu' = 0.623$. This finding suggests a possible breakdown of Equation ([11]) for very high melt numbers for ice/basalt impacts. Still, though, $\mu' = 0.623$ remains significantly lower than the $\mu' = 0.819$ from Barr & Citron ([2011]). In Section [4], we opt to use $a = -0.890$ and $\mu' = 0.535$. However, the uncertainty on μ' indicates that a dedicated investigation of melt volume scaling would be useful, specifically, ice projectiles under different EoS specifications, impacting various target materials at a range of velocities.

5.5. Conclusion

In searching for craters produced by ISOs impacting terrestrial bodies, it is important to have a set of criteria that differentiate these craters from those produced by asteroids and comets. By analyzing local stellar kinematics, we show that ISOs that encounter the solar system at speeds of $\geqslant 100$ km s^{-1} impact the Moon and Mars at rates of ~ 0.09 and ~ 0.29 Gyr^{-1}, respectively. Importantly, 100 km s^{-1} exceeds the impact speeds of most small solar system objects. Therefore, crater properties that depend strongly on impact speed may be especially pertinent. Transient crater dimensions are expected to obey late-stage equivalence. We compare two hydro simulations to show that it is difficult to distinguish simple craters formed by high- and low-speed impacts. Melt volume, on the other hand, does not follow the point-source limit (Pierazzo et al. [1997]) and offers a possible avenue for identifying high-speed craters. This approach requires overcoming degeneracies with impact angle and target composition and obtaining precise estimates of the melt volume. Alternatively, vapor condensate composition and spherule dimensions could be revealing of extremely fast impacts. Facilitated by upcoming crewed and robotic Moon missions, identifying ISO craters may soon be feasible through in situ or return analyses of impact crater samples.

Appendix A
Diameter Scaling Validation for Basalt/Basalt Impacts

We perform additional simulations of a basalt projectile impacting a nearly cohesionless basalt target with $\Phi = 12\%$ and $f = 0.6$. These simulations serve as a foil to the ice projectile and allow us to verify our simulation setup by independently measuring the associated transient diameter scaling relation, which was also measured by Prieur et al. ([2017]). Since these
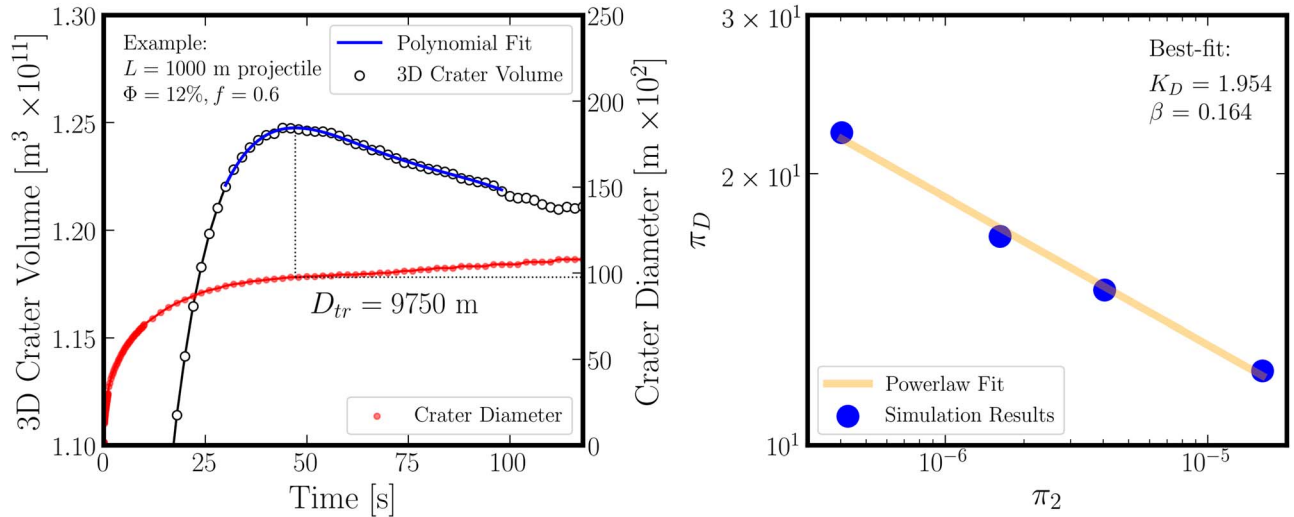
Figure 6. Crater scaling relation for basalt-on-basalt impacts, which serves as verification of our simulation setup. Left: determination of transient crater diameter for the simulation involving a 1000 m diameter projectile. A fifth-degree polynomial is fit to the crater dimensions near maximum volume. The diameter that maximizes the polynomial is taken as $D_{\rm tr}$. Right: best-fit power law plotted against dimensionless π-scaling quantities for the four simulations considered.

craters are in the gravity-dominated regime, Equation (C1) dictates the transient crater diameter. The impact speed was held constant at $v_i = 12.7$ km s^{-1}, while the projectile diameter took values of $L = 25$, 100, 250, and 1000 m. Prieur et al. (2017) defined $D_{\rm tr}$ as the crater diameter at the time of maximum crater volume. In our simulations, the crater volume as a function of time made discrete jumps as the crater grew in the extension zones. In order to make our measurement more robust to the spatial resolution, we fit a fifth-degree polynomial to the volume as a function of time near its maximum value. We took the time at which the polynomial reaches its maximum as defining the transient crater. Finally, we linearly interpolated the crater diameter between neighboring time stamps to obtain $D_{\rm tr}$. The crater diameter was measured at the level of the preimpact surface. The polynomial fit only included points within 2.5% of the maximum crater volume, which helped exclude late-time data where the crater volume changes due to modification processes. Figure 6 shows a schematic of this process (left panel) and our results (right panel).

Our best-fit parameters are $K_D = 1.954$ and $\beta = 0.164$, which agree well with the scaling from Prieur et al. (2017), $K_D = 1.984$ and $\beta = 0.165$. The values for π_D predicted by our scaling relation and that of Prieur et al. (2017) disagree by <3% for each of the projectiles we considered; this slight disagreement may be due to different zoning and resolution schemes in the simulation setups (e.g., we use a smaller high-resolution zone than Prieur et al. 2017, the layer assigned to zero depth may be different, and cell sizes in the extension zone may also be different).

Simulations in the strength-dominated regime (high target cohesion) required a different approach for measuring $D_{\rm tr}$. In these cases, the crater volume grew during excavation and then plateaued, as opposed to reaching a maximum and subsequently decreasing. The crater diameter followed a similar trend. For these simulations, we select all time stamps in which the crater diameter is within 10% of its diameter at the last simulation time stamp and subsequently take the median of these diameters as a measurement of $D_{\rm tr}$.

Appendix B
Melt Volume Dependency on CPPR

The simulations in this study were conducted at a resolution of 20 CPPR, which was a compromise between simulation run time and accuracy. Barr & Citron (2011) found that near 20 CPPR, dunite/dunite impacts at 20 km s^{-1} underestimate the melt volume by ~15%. Since this study concerns different materials and impact speeds, we performed additional simulations to determine the melt volume's dependence on CPPR. We simulated 40 m ice projectiles impacting (cohesionless) basalt targets at 10, 30, and 100 km s^{-1} at five different resolutions. Our results are depicted in Figure 7. The volume of melt (plus vapor) was subsequently determined using the basalt complete melting pressure $P_c = 106$ GPa (Quintana et al. 2015). In the 30 km s^{-1} scenario, melt volume is underestimated by 45%, 22%, 8.3%, and 2.9% for 10, 20, 40, and 60, respectively (compared to 80 CPPR). In the 100 km s^{-1} scenario, melt volume is underestimated by 38%, 19%, 7%, and 2.5% for 10, 20, 40, and 60, respectively (again, compared to 80 CPPR). We found the 10 km s^{-1} impact simulations do not produce any melt at 80 CPPR or lower resolution. In our main analysis, we multiply melt volume by 1.28 and 1.23 in the 30 and 100 km s^{-1} scenarios, respectively, to account for the resolution dependence.
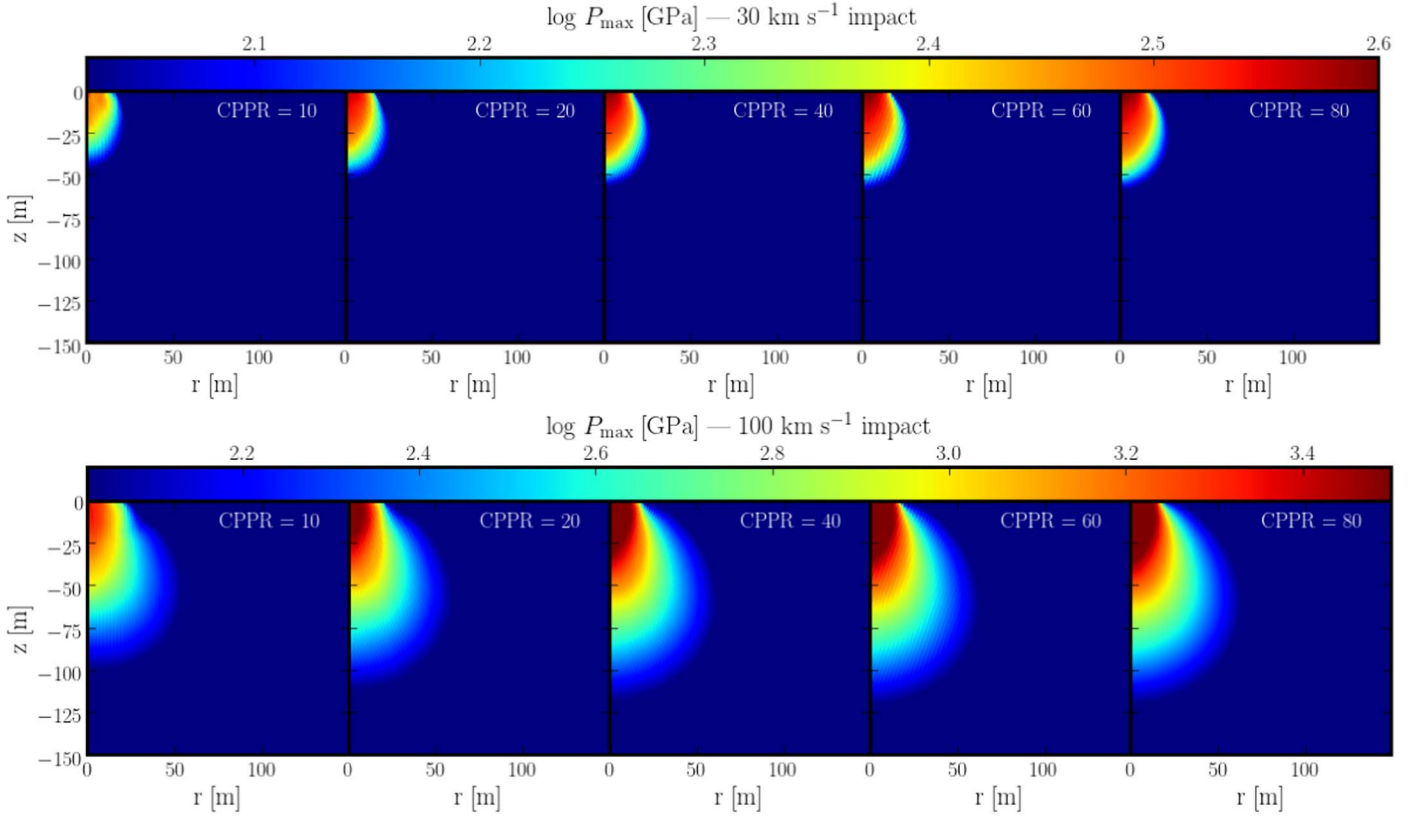
Figure 7. Dependence of maximum pressure on simulation resolution for the nominal simulation setup in this study (ice projectile striking a cohesionless basalt target). Each panel depicts the original locations of tracer particles embedded in the high-resolution zone of the simulation, color coded by the maximum pressure they experience following the impact. The top row shows results for a 30 km s^{-1} impact, whereas the bottom row is for a 100 km s^{-1} impact. The CPPR takes values of 10, 20, 40, 60, and 80. Note that the color scales for the top and bottom rows have different maxima but the same minima at 106 GPa (Quintana et al. 2015).

Appendix C
Analytic Melt Volume Scaling

As follows, we combine Pi-group scaling for a crater's transient diameter (Equation (10)) with a melt volume scaling relation (Equation (11)) valid for $v_i^2/E_M \gtrsim 30$ (Pierazzo et al. 1997). Together, they break the degeneracy between projectile impact velocity and projectile size. While a useful demonstration, this analysis neglects impact angle dependence and detailed target lithology. For simple craters formed in granular targets, Equation (10)'s dependence on π_3 is negligible, and the relation follows

$$\pi_D = K_1 \pi_2^{-\mu/(2+\mu)} \pi_4^{(2+\mu-6\nu)/(6+3\mu)} \qquad (C1)$$

for an empirically determined constant K_1. The variables μ and ν follow from the point-source coupling constant in Equation (5). They are often determined experimentally, and μ typically lies between energy and momentum scaling ($\mu = 2/3$ and $1/3$). Let $\beta \equiv \mu/(2+\mu)$ and $\eta \equiv (2+\mu-6\nu)/(6+3\mu)$ to simplify notation. Next, consider the scaling relation used by Cintala & Grieve (1998), which follows from expanding Equation (C1) and multiplying both sides of the equation by the cube-root of the projectile volume:

$$D_{tr} = \frac{K_1}{2}\left(\frac{4\pi}{3}\right)^{(1-\beta)/3}\left(\frac{\rho_t}{\rho_p}\right)^{\eta-1/3}$$
$$\times\ L^{1-\beta}g^{-\beta}v_i^{2\beta}. \qquad (C2)$$

After calculating melt volumes from hydrocode simulations, they found a power-law relationship for melt volume that depends strongly on D_{tr} and weakly on v_i. By assuming the projectile is spherical, one may restate Equation (11) as

$$V_M = \frac{k\pi}{6}L^3\left(\frac{v_i^2}{E_M}\right)^{3\mu'/2}. \qquad (C3)$$

Finally, combining Equations (C2) and (C3), and in the process removing the L dependence, we arrive at

$$V_M = \frac{k}{8}\left(\frac{K_1}{2}\right)^{-3/(1-\beta)}D_{tr}^{3/(1-\beta)}$$
$$\times\left(\frac{\rho_t}{\rho_p}\right)^{(1-3\eta)/(1-\beta)}E_M^{-3\mu'/2}v_i^{3\mu'-6\beta/(1-\beta)}$$
$$\times\ g^{3\beta/(1-\beta)}. \qquad (C4)$$

Similarly, we can derive a relationship between melt volume, transient crater diameter, and impact velocity in the case of strength-dominated craters. We start with

$$\pi_D = K_1 K_2^{-\mu/2}\pi_3^{-\mu/2}\pi_4^{(1-3\nu)/3}. \qquad (C5)$$

This equation involves a separate, empirically determined constant (K_2) and the same scaling variables as above. To simplify notation, let $\alpha \equiv \mu/2$ and $\xi \equiv (1-3\nu)/3$. Then,

$$D_{tr} = \frac{K_1}{2}\left(\frac{4\pi}{3}\right)^{1/3}\left(\frac{\rho_t}{\rho_p}\right)^{\xi-1/3}\left(\frac{\rho_t}{K_2 Y}\right)^{\alpha}Lv_i^{2\alpha}. \qquad (C6)$$

Combining the above equation with Equation (C3) yields

$$V_M = \frac{k}{8}\left(\frac{K_1}{2}\right)^{-3} D_{tr}^3 \left(\frac{\rho_t}{\rho_p}\right)^{-3\xi+1} \left(\frac{K_2 Y}{\rho_t}\right)^{3\alpha}$$
$$\times E_M^{-3\mu'/2} v_i^{3\mu'-6\alpha}. \tag{C7}$$

Equations (C4) and (C7) describe the theoretical amount of melt volume in gravity- and strength-dominated craters, respectively, accounting for different projectile and target bulk densities. Again, we emphasize that impact angle and lithology other than bulk density could influence the actual melt volume. Nevertheless, these equations give the baseline feasibility of determining a projectile's impact speed from measurements of its crater.

ORCID iDs

Samuel H. C. Cabot ⓘ https://orcid.org/0000-0001-9749-6150
Gregory Laughlin ⓘ https://orcid.org/0000-0002-3253-2621

References

Abramov, O., Wong, S. M., & Kring, D. A. 2012, Icar, 218, 906
Amsden, A. A., Ruppel, H. M., & Hirt, C. W. 1980, SALE: a simplified ALE computer program for fluid flow at all speeds, US Dept. of Energy doi:10.2172/5176006
Anderson, E., & Francis, C. 2012, AstL, 38, 331
Anguiano, B., Majewski, S. R., Freeman, K. C., Mitschang, A. W., & Smith, M. C. 2017, MNRAS, 474, 854
Artemieva, N., & Ivanov, B. 2004, Icar, 171, 84
Artemieva, N., & Pierazzo, E. 2009, M&PS, 44, 25
Artemieva, N., & Pierazzo, E. 2011, M&PS, 46, 805
Barr, A. C., & Citron, R. I. 2011, Icar, 211, 913
Barton, P., Grieve, R., Morgan, J., et al. 2010, Large Meteorite Impacts and Planetary Evolution IV (Boulder, CO: Geological Society of America)
Binney, J., & Tremaine, S. 2008, Galactic Dynamics: Second Edition (Princeton, NJ: Princeton Univ. Press)
Birkhoff, G., MacDougall, D. P., Pugh, E. M., & Taylor, Geoffrey, S. 1948, JAP, 19, 563
Bjorkman, M. D., & Holsapple, K. A. 1987, IJIE, 5, 155
Bodewits, D., Noonan, J. W., Feldman, P. D., et al. 2020, NatAs, 4, 867
Bond, N. A., Ivezić, Ž., Sesar, B., et al. 2010, ApJ, 716, 1
Bowling, T., Johnson, B., Wiggins, S., et al. 2020, Icar, 343, 113689
Buckingham, E. 1914, PhRv, 4, 345
Cintala, M. J., & Grieve, R. A. F. 1998, M&PS, 33, 889
Collins, G., Melosh, H., & Wünnemann, K. 2011, IJIE, 38, 434
Collins, G. S. 2014, JGRE, 119, 2600
Collins, G. S., Patel, N., Davison, T. M., et al. 2020, NatCo, 11, 1480
Collins, G. S., Wünnemann, K., Artemieva, N., & Pierazzo, E. 2012, Numerical Modelling of Impact Processes (Hoboken, NJ: Wiley), 254
Davison, T. M., Collins, G. S., Elbeshausen, D., Wünnemann, K., & Kearsley, A. 2011, M&PS, 46, 1510
Dehnen, W., & Binney, J. J. 1998, MNRAS, 298, 387
Denton, C. A., Johnson, B. C., Wakita, S., et al. 2021, GeoRL, 48, e91596
Desch, S. J., & Jackson, A. P. 2021, JGRE, 126, e06706
Dienes, J. K., & Walsh, J. M. 1970, High-Velocity Impact Phenomena (New York: Academic Press, Inc.), 46
Do, A., Tucker, M. A., & Tonry, J. 2018, ApJL, 855, L10
Dybczyński, P. A., Królikowska, M., & Wysoczańska, R. 2019, arXiv:1909.10952
Elbeshausen, D., WÃ?nnemann, K., & Collins, G. S. 2009, Icar, 204, 716
Engelhardt, T., Jedicke, R., Vereš, P., et al. 2017, AJ, 153, 133
Eubanks, T. M., Hein, A. M., Lingam, M., et al. 2021, arXiv:2103.03289
Francis, C., & Anderson, E. 2009, NewA, 14, 615
French, B. M. 1998, Traces of Catastrophe: A Handbook of Shock-Metamorphic Effects in Terrestrial Impact Structures (Houston, TX: Lunar and Planetary Inst.), 954
Füglistaler, A., & Pfenniger, D. 2018, A&A, 613, A64
Gaia Collaboration, Katz, D., Antoja, T., et al. 2018, A&A, 616, A11
Gaia Collaboration, Smart, R. L., Sarro, L. M., et al. 2021, A&A, 649, A6

Grieve, R. A. F. 1987, AREPS, 15, 245
Grieve, R. A. F., & Cintala, M. J. 1982, LPSC, 2, 1607
Gulick, S., Christeson, G., Barton, P., et al. 2013, RvGeo, 51, 31
Guzik, P., Drahus, M., Rusek, K., et al. 2020, NatAs, 4, 53
Head, J. N., Melosh, H. J., & Ivanov, B. A. 2002, Sci, 298, 1752
Holsapple, K. A., & Schmidt, R. M. 1982, JGR, 87, 1849
Holsapple, K. A., & Schmidt, R. M. 1987, JGR, 92, 6350
Housen, K. R., & Holsapple, K. A. 2011, Icar, 211, 856
Ivanov, B., Deniem, D., & Neukum, G. 1997, IJIE, 20, 411
Jewitt, D., & Luu, J. 2019, ApJL, 886, L29
Johnson, B. C., Bowling, T. J., Trowbridge, A. J., & Freed, A. M. 2016, GeoRL, 43, 10068
Johnson, B. C., & Melosh, H. J. 2012a, Icar, 217, 416
Johnson, B. C., & Melosh, H. J. 2012b, Natur, 485, 75
Joy, K. H., Crawford, I. A., Curran, N. M., et al. 2016, EM&P, 118, 133
Keller, L. P., & McKay, D. S. 1992, LPSC, 22, 137
Kiefer, W. S., Macke, R. J., Britt, D. T., Irving, A. J., & Consolmagno, G. J. 2012, GeoRL, 39, L07201
Kieffer, S. W., & Simonds, C. H. 1980, RvGSP, 18, 143
Lacki, B. C. 2021, ApJ, 919, 8
Le Feuvre, M., & Wieczorek, M. A. 2008, Icar, 197, 291
Le Feuvre, M., & Wieczorek, M. A. 2011, Icar, 214, 1
Levine, J., Becker, T. A., Muller, R. A., & Renne, P. R. 2005, GeoRL, 32, L15201
Levine, W. G., Cabot, S. H. C., Seligman, D., & Laughlin, G. 2021, ApJ, 922, 39
Mamajek, E. 2017, RNAAS, 1, 21
Marchetti, T. 2021, MNRAS, 503, 1374
McKay, D. S. 1991, in Lunar Sourcebook, A User's Guide to the Moon, ed. G. H. Heiken, D. T. Vaniman, & B. M. French (Cambridge: Cambridge Univ. Press)
Meech, K. J., Weryk, R., Micheli, M., et al. 2017, Natur, 552, 378
Melosh, H. J. 1989, Impact Cratering : A Geologic Process (New York: Oxford Univ. Press), 126
Melosh, H. J. 2007, M&PS, 42, 2079
Melosh, H. J., & Collins, G. S. 2005, Natur, 434, 157
Melosh, H. J., Ryan, E. V., & Asphaug, E. 1992, JGR, 97, 14735
Micheli, M., Farnocchia, D., Meech, K. J., et al. 2018, Natur, 559, 223
Naney, M. T., Crowl, D. M., & Papike, J. J. 1976, LPSC, 7, 155
Nataf, H.-C. 2000, AREPS, 28, 391
Nissen, P. E. 2004, in Carnegie Observatories Centennial Symposia IV. Origin and Evolution of the Elements, ed. A McWilliam & M. Rauch (Cambridge: Cambridge Univ. Press), 154
Nordström, B., Mayor, M., Andersen, J., et al. 2004, A&A, 418, 989
O'Brien, D. P., & Sykes, M. V. 2011, SSRv, 163, 41
Ohnaka, M. 1995, GeoRL, 22, 25
Okeefe, J. D., & Ahrens, T. J. 1977, LPSC, 3, 3357
Pierazzo, E., Artemieva, N., Asphaug, E., et al. 2008, M&PS, 43, 1917
Pierazzo, E., Artemieva, N., & Ivanov, B. 2005, Large Meteorite Impacts III (Boulder, CO: Geological Society of America)
Pierazzo, E., & Melosh, H. 2000, Icar, 145, 252
Pierazzo, E., Vickery, A. M., & Melosh, H. J. 1997, Icar, 127, 408
Plescia, J. B., Barnouin, O., & Stopar, J. 2014, LPSC, 45, 2141
Prieur, N. C., Rolf, T., Luther, R., et al. 2017, JGRE, 122, 1704
Prieur, N. C., Rolf, T., Wünnemann, K., & Werner, S. C. 2018, JGRE, 123, 1555
Quintana, S., Crawford, D., & Schultz, P. 2015, Procedia Engineering, 103, 499
Rafikov, R. R. 2018, ApJL, 867, L17
Recio-Blanco, A., de Laverny, P., Kordopatis, G., et al. 2014, A&A, 567, A5
Reid, A. M., Lofgren, G. E., Heiken, G. H., Brown, R. W., & Moreland, G. 1973, EOSTr., 54, 606
Rojas-Arriagada, A., Recio-Blanco, A., Hill, V., et al. 2014, A&A, 569, A103
Sandage, A., & Fouts, G. 1987, AJ, 93, 74
Schaber, G. G., Strom, R. G., Moore, H. J., et al. 1992, JGR, 97, 13257
Schenk, P. M., Chapman, C. R., Zahnle, K., & Moore, J. M. 2004, in Jupiter. The Planet, Satellites and Magnetosphere, ed. F. Bagenal, T. E. Dowling, & W. B. McKinnon (Cambridge: Cambridge Univ. Press), 427
Schmidt, R. M., & Housen, K. R. 1987, IJIE, 5, 543
Schönrich, R., Binney, J., & Dehnen, W. 2010, MNRAS, 403, 1829
Schultz, P. H., & Gault, D. E. 1985, JGR, 90, 3701
Schwarzschild, K. 1907, Göttingen Nachr. Math.-Phys. Kl, 3, 614
Seligman, D., & Laughlin, G. 2018, AJ, 155, 217
Seligman, D., & Laughlin, G. 2020, ApJL, 896, L8
Seligman, D., Laughlin, G., & Batygin, K. 2019, ApJL, 876, L26
Shu, F. H. 1969, ApJ, 158, 505

Silber, E. A., Zanetti, M., Osinski, G. R., Johnson, B. C., & Grieve, R. A. F. 2018, LPSC, 49, 1401

Smit, J., Alvarez, W., Montanari, A., et al. 1992, LPSC, 22, 87

Snodgrass, C., & Jones, G. H. 2019, NatCo, 10, 5418

Steel, D. 1998, P&SS, 46, 473

Stromgren, B. 1987, in The Galaxy, Proc. of the NATO Advanced Study Inst., Vol. 207, ed. G. Gilmore & B. Carswell (Dordrecht: Reidel), 229

Stöeffler, D. 1972, Fortschritte der Mineralogie, 49, 50

Svetsov, V. V., & Shuvalov, V. V. 2015, P&SS, 117, 444

Tagle, R. 2005, LPSC, 36, 2008

Tagle, R., & Hecht, L. 2006, M&PS, 41, 1721

Trilling, D. E., Robinson, T., Roegge, A., et al. 2017, ApJL, 850, L38

Venn, K. A., Irwin, M., Shetrone, M. D., et al. 2004, AJ, 128, 1177

Warren, P. H. 2008, GeCoA, 72, 3562

Warren, P. H., Young, E. D., & Newman, W. I. 2008, LPI Contribution, 1415, 2123

Wieczorek, M. A., Neumann, G. A., Nimmo, F., et al. 2013, Sci, 339, 671

Wu, J., Milkereit, B., & Boerner, D. E. 1995, JGR, 100, 4117

Wünnemann, K., Collins, G., & Melosh, H. 2006, Icar, 180, 514

Wünnemann, K., Collins, G., & Osinski, G. 2008, E&PSL, 269, 530

Wünnemann, K., Nowka, D., Collins, G., Elbeshausen, D., & Bierhaus, M. 2011, in Proc. of the 11th Hypervelocity Impact Symp., 2010

Yamamoto, S., Hasegawa, S., Suzuki, A. I., & Matsunaga, T. 2017, JGRE, 122, 1077

Zeng, X., Zuo, W., Zhang, Z., Liu, Y., & Li, C. 2017, EGU General Assembly, EGU2017, 19, 2026